Dynamics of human protein kinases linked to drug selectivity

Warintra Pitsawong[*,a], Vanessa Buosi[*,a], Renee Otten[*,a], Roman V. Agafonov[*,a] Adelajda Zorba[a], Nadja Kern[a], Steffen Kutter[a], Gunther Kern[a], Ricardo A. P. Pádua[a], Xavier Meniche[b], and Dorothee Kern[#,a]

[a]*Department of Biochemistry and Howard Hughes Medical Institute, Brandeis University, Waltham, MA 02452, USA*

[b]*Department of Microbiology and Physiological Systems, University of Massachusetts Medical School, Worcester, MA 01605, USA*

*these authors contributed equally to this work

#corresponding author

Abstract

Protein kinases are major drug targets, but the development of highly-selective inhibitors has been challenging due to the similarity of their active sites. The observation of distinct structural states of the fully-conserved Asp-Phe-Gly (DFG) loop has put the concept of conformational selection for the DFG-state at the center of kinase drug discovery. Recently, it was shown that Gleevec selectivity for the Tyr-kinases Abl was instead rooted in conformational changes after drug binding. Here, we investigate whether protein dynamics after binding is a more general paradigm for drug selectivity by characterizing the binding of several approved drugs to the Ser/Thr-kinase Aurora A. Using a combination of biophysical techniques, we propose a universal drug-binding mechanism, that rationalizes selectivity, affinity and long on-target residence time for kinase inhibitors. These new concepts, where protein dynamics in the drug-bound state plays the crucial role, can be applied to inhibitor design of targets outside the kinome.

eLife digest

The Ser/Thr kinase Aurora A is an important target for the development of new anticancer therapies. A longstanding question is how to specifically and effectively inhibit only this kinase in a background of over 550 protein kinases with very similar structures. To this end, understanding the inhibition mechanism of Aurora A by different drugs is essential. Here, we characterize the kinetic mechanism of three distinct kinase drugs, Gleevec (Imatinib), Danusertib (PHA739358) and AT9283 (Pyrazol-4-yl Urea) for Aurora A. We show that inhibitor affinities do not rely exclusively on the recognition of a specific conformation of the Asp-Phe-Gly loop of the kinase.

Our quantitative kinetics data put forward an opposing mechanism in which a slow conformational change after drug binding (i.e., induced-fit step) dictates drug affinity.

Introduction

Protein kinases have become the number one drug target of the 21th century (Cohen, 2002; Hopkins & Groom, 2002), due to their central role in cellular processes and involvement in various types of cancer (Carvajal, Tse, & Schwartz, 2006; Gautschi et al., 2008; Katayama & Sen, 2010). Despite their therapeutic significance, the development of specific kinase inhibitors proves to be extremely challenging because they must discriminate between the very similar active sites of a large number of kinases in human cells. One of the biggest success stories is Gleevec: a highly selective drug that specifically targets Abl kinase, providing an efficient treatment of chronic myelogenous leukemia (CML) and minimizing side effects (Iqbal & Iqbal, 2014). Despite being a multi-billion-dollar cancer drug, the mechanism responsible for its impressive selectivity has been elusive until recently. It has long been proposed that the conformational state of the fully conserved DFG (for Asp-Phe-Gly) loop (Taylor, Keshwani, Steichen, & Kornev, 2012) dictates the selectivity for Gleevec and other kinase inhibitors (Lovera et al., 2012; Treiber & Shah, 2013). Recent quantitative binding kinetics put forward an opposing mechanism in which an induced-fit step after drug binding is responsible for Gleevec's selectivity (Agafonov, Wilson, Otten, Buosi, & Kern, 2014; Wilson et al., 2015).

Here we ask the question whether this fundamentally different mechanism is a more general principle for drug efficacy and selectivity not only for Tyr kinases such as Abl, but also for Ser/Thr kinases. To this end, we chose the Ser/Thr kinase Aurora A and investigated the binding kinetics of three distinct kinase drugs: Danusertib, AT9283, and Gleevec. Aurora A kinase is one of the key regulators of mitotic events, including mitotic entry, centrosome maturation and spindle formation (Fu, Bian, Jiang, & Zhang, 2007; Lukasiewicz & Lingle, 2009; Marumoto, Zhang, & Saya, 2005), as well as assisting in neuronal migration (Nikonova, Astsaturov, Serebriiskii, Dunbrack, & Golemis, 2013). Aurora A has attracted significant attention for the development of targeted agents for cancer because it is overexpressed in a wide range of tumors, including breast, colon, ovary and skin malignancies (Carvajal et al., 2006; Gautschi et al., 2008; Katayama & Sen, 2010; Lok, Klein, & Saif, 2010; Marzo & Naval, 2013). The focus was mainly on ATP-competitive inhibitors, but more recently inhibition by allosteric compounds has also been pursued with the aim of achieving higher selectivity (Asteriti et al., 2017; Bayliss, Burgess, & McIntyre, 2017; Burgess et al., 2016; Janecek et al., 2016; McIntyre et al., 2017). So far, only the clinical significance of Aurora A inhibition by ATP-competitive drugs has been established (Bavetsias &

Linardopoulos, 2015; Borisa & Bhatt, 2017), but little is known about their binding mechanisms. Many high-resolution X-ray structures of Aurora A kinase bound to different inhibitors have been solved (Bavetsias et al., 2015; Dodson et al., 2010; Fancelli et al., 2006; Ferguson et al., 2017; Heron et al., 2006; Howard et al., 2009; Kilchmann et al., 2016; Martin et al., 2012; Zhao et al., 2008), but the selectivity profile of those kinase inhibitors remains very difficult to explain.

The drugs used in this study are small, ATP-competitive inhibitors. Danusertib (PHA739358) and AT9283 were developed for Aurora kinases, whereas Gleevec is selective for the Tyr kinase Abl. Danusertib inhibits all members of the Aurora family with low nanomolar IC_{50} values (13, 79 and 61 nM for Aurora A, B and C, respectively) (Carpinelli et al., 2007; Fraedrich et al., 2012) and was one of the first Aurora kinase inhibitors to enter phase I and II clinical trials (Kollareddy et al., 2012; Steeghs et al., 2009). A crystal structure of Danusertib bound to Aurora A kinase shows an inactive kinase with the DFG-loop in the *out* conformation (Fancelli et al., 2006). AT9283 inhibits both Aurora A and B with an IC_{50} of 3 nM (Howard et al., 2009) and has also entered several clinical trials (Borisa & Bhatt, 2017). Interestingly, the crystal structure of Aurora A with AT9283 shows that this drug binds to the DFG-*in*, active conformation of the kinase (Howard et al., 2009). Both drugs are high-affinity binders that reportedly bind to a discrete kinase conformation and would allow us to probe for a conformational-selection step. Lastly, we selected Gleevec as a drug that is not selective for Aurora A and should, therefore, have a weaker binding affinity. We reasoned that this choice of inhibitors could reveal general mechanisms underlying drug selectivity and affinity.

The combination of X-ray crystallography, NMR spectroscopy and comprehensive analysis of drug binding and release kinetics delivered a general mechanistic view. Differential drug affinity is not rooted in the overwhelmingly favored paradigm of the DFG-conformation, but instead in the dynamic personality of the kinase that is manifested in conformational changes after drug binding. Notably, such conformational changes have evolved for its natural substrates, and the drugs take advantage of this built-in protein dynamics.

Results

Dephosphorylated Aurora A samples both an inactive and active structure

A plethora of X-ray structures and functional assays led to the general notion that dephosphorylated Aurora A and, more universally, Ser/Thr kinases are in an inactive conformation and that phosphorylation or activator binding induces the active structure. A comparison of many X-ray structures of inactive and active forms of Ser/Thr kinases resulted in an elegant proposal of the structural hallmarks for the active state by Taylor and collaborators:

the completion of both the regulatory and catalytic spines spanning the N- and C-terminal domains, including the orientation of the DFG-motif (Kornev & Taylor, 2010, 2015).

To our surprise, two crystals from the same crystallization well capture both the inactive and active conformations of dephosphorylated Aurora A bound with AMPPCP (Figure 1A, B). As anticipated, the first structure (PDB 4C3R (Zorba et al., 2014)) superimposes with the well-known inactive, dephosphorylated Aurora A structure (PDB 1MUO (Cheetham et al., 2002)) and the activation loop is not visible as commonly observed for kinases lacking phosphorylation of the activation loop (Zorba et al., 2014). Unexpectedly, the second structure (PDB 6CPF; Figure 1-*figure supplement 1*) adopts the same conformation as the previously published phosphorylated, active structure (PDB 1OL7 (Bayliss, Sardon, Vernos, & Conti, 2003)) (Figure 1C) and the first part of the activation loop could be built, although the B-factors are high. Every hallmark of an active state is seen for this dephosphorylated protein, including the DFG-*in* conformation that is essential for completing the regulatory spine. In contrast, the DFG-loop is in the *out* position for the inactive form of Aurora A (Figure 1D, cyan). In the active, non-phosphorylated structure, electron density is seen in the canonical tighter Mg^{2+}-binding site, where the metal ion is coordinated to the $\alpha-$ and β-phosphates of AMPPCP and Asp274. The presence of the metal is supported by the CheckMyMetal (Zheng et al., 2017) validation except that the coordination is incomplete. We surmise that two water molecules, not visible in our data, complete the coordination sphere as is seen in several higher-resolution structures. In the inactive structure, no electron density for Mg^{2+} can be identified possibly due to the fact that Asp274 is rotated to the DFG-*out* position and is, therefore, lost as coordination partner. Furthermore, sampling of the active conformation does not depend on AMPPCP binding as dephosphorylated, apo Aurora A also crystallizes in the active form (PDB 6CPE; Figure 1E, F and Figure 1-*figure supplement 1*).

We note that in Aurora kinase sequences a tryptophan residue, Trp277, is immediately following the DFG motif and displays a drastically different orientation whether Aurora A is in an active (DFG-*in*) or inactive (DFG-*out*) conformation (Figure 1D). This Trp moiety is unique for the Aurora kinase family in the Ser/Thr kinome and its position is suggested to be important for tuning the substrate specificity (C. Chen et al., 2014). We used this Trp residue as probe to monitor the DFG flip and drug binding in real time as described below.

The fact that the inactive and active states are seen in the crystal implies that both are sampled; however, it does not deliver information about the relative populations or interconversion rates. Therefore, we set out to monitor the conformational exchange of the DFG-*in*/*out* flip in solution. Owing to the reported importance of the DFG flip for activity, regulation and drug design, there have been extensive efforts to characterize this conformational equilibrium by computation

(Badrinarayan & Sastry, 2014; Barakat et al., 2013; Meng, Lin, & Roux, 2015; Sarvagalla & Coumar, 2015). As an experimental approach, NMR spectroscopy is an obvious choice; however efforts on several Ser/Thr and Tyr kinases led to the general conclusion that the activation loop, including the DFG motif and most of the active-site residues, cannot be detected due to exchange broadening, and at best can only be seen after binding of drugs that stabilize conformations (Campos-Olivas, Marenchino, Scapozza, & Gervasio, 2011; Langer et al., 2004; Vajpai et al., 2008; Vogtherr et al., 2006).

[^{1}H-^{15}N]-HSQC experiments on uniformly ^{15}N-labeled samples of Aurora A proved to be no exception: many peaks are missing and only three out of four tryptophan side chain indole signals are seen in the 2D spectra of a [^{15}N]-Trp labeled sample (Figure 2A, B). Therefore, we sought a strategy to overcome this general problem of exchange broadening that hampers the detection of the DFG equilibrium. Aurora A was produced containing 5-fluoro-tryptophan residues to allow for one-dimensional ^{19}F spectroscopy to deal with exchange broadening while providing sensitivity close to proton NMR (Kitevski-LeBlanc & Prosser, 2012). Now, we observe as expected four peaks in our NMR spectra for apo- and AMPPCP-bound wild-type Aurora A (Figure 2C). A deconvolution of the spectrum yields almost identical integral values for all four peaks, whereas the linewidth of one resonance is approximately 5-fold larger (Figure 2D, purple signal). This broad peak is a prime candidate to originate from Trp277, directly adjacent to the DFG-loop. The W277L mutation confirmed our hypothesis (Figure 2C), and the extensive line broadening of this signal in a one-dimensional spectrum is consistent with its absence in the [^{1}H,^{15}N]-HSQC spectrum. Of note, the W277L mutant is still active, as confirmed by a kinase assay, most likely because this Trp is not conserved in Ser/Thr kinases, where a Leu residue is found at the position for several Ser/Thr family members. Mutating any of the other, more conserved Trp residues resulted in insoluble proteins. The broad line shape for the Trp277 peak hints at severe exchange broadening in the surrounding of the DFG-loop and is consistent with the high B-factors for Trp277 and its neighboring residues observed in all crystal structures described here. Determination of relative populations and rate constants of interconversion is not possible from this data, but this missing piece of information was obtained by stopped-flow kinetics of drug binding.

Gleevec binding to Aurora A distinguishes conformational selection versus induced-fit mechanisms

Through groundbreaking experiments on the Tyr kinases Abl and Src, the concept of drug selectivity based on the DFG-loop conformation has received considerable attention in kinase drug discovery (Lovera et al., 2012; Treiber & Shah, 2013). A recent report provides kinetic

evidence for such conformational selection, but identifies an induced-fit step after drug binding as the overwhelming contribution for Gleevec selectivity towards Abl compared to Src (Agafonov et al., 2014). Here, we ask the obvious question if this mechanism of Gleevec binding to Abl might exemplify a more general mechanism for kinase inhibitors.

To assess which kinetic steps control drug affinity and selectivity, we first studied the binding kinetics for Gleevec to Aurora A by stopped-flow spectroscopy using intrinsic tryptophan fluorescence under degassing conditions to reduce photobleaching. At 25 °C, the binding of Gleevec to Aurora A was too fast to be monitored and, therefore, experiments were performed at 10 °C. Binding kinetics of Gleevec to Aurora A exhibited biphasic kinetic traces (Figure 3A). The first, fast phase is characterized by a decrease in the fluorescence intensity (Figure 3A, B), with an observed rate constant, k_{obs}, increasing linearly with Gleevec concentration (Figure 3C). The slope corresponds to the bimolecular rate constant, k_2 = (1.1 ± 0.3) × 10^6 $M^{-1}s^{-1}$, of Gleevec binding to Aurora A and the dissociation of Gleevec is determined from the intercept, k_{-2} = 31 ± 2 s^{-1} (Figure 3C). The second, slow phase exhibits an increase in fluorescence intensity (Figure 3A), with the observed rate constant decreasing with Gleevec concentration (Figure 3D). The decreasing k_{obs} provides unequivocal evidence of conformational selection, where its rate of interconversion is slower than the rate of ligand dissociation ($k_1 + k_{-1} \ll k_{-2}$). The values of k_1 and k_{-1} can be estimated by fitting the data to Equation 1 and are 0.014 ± 0.001 s^{-1} and 0.011 ± 0.002 s^{-1}, respectively (Figure 3D). These rate constants represent the conformational change from DFG-*in* to -*out* and vice versa since Gleevec is a DFG-*out* selective inhibitor due to steric hindrance (Nagar et al., 2002; Schindler et al., 2000; Seeliger et al., 2007).

In order to more rigorously analyze the data and test the model, all time courses of the fluorescence changes were globally fit using the microscopic rate constants determined above as starting values (Figure 4) to the model in Figure 3G, where also the resulting microscopic rate constants are given. The lack of a conformational transition after drug binding (i.e., induced-fit step) in Aurora A should dramatically decrease drug affinity in comparison to Abl. Indeed, Gleevec binds to Aurora A with a K_D of 24 ± 7 µM (Figure 3F) compared to the low nM affinity to Abl (Agafonov et al., 2014). Two pieces of independent evidence establish that there is indeed no induced-fit step in Gleevec binding to Aurora A: (i) the calculated K_D from the kinetic scheme is in agreement with the macroscopically measured K_D (*c.f.* Figure 3G and 3F), and (ii) the observed k_{off} from the dilution experiment (Figure 3E) coincides with the physical dissociation rate (i.e., intercept of the binding plot, 31 ± 2 s^{-1}, in Figure 3C). In summary, the lack of an induced-fit step

for Gleevec binding to Aurora A is the major reason for Gleevec's weak binding, and not the DFG-loop conformation.

Kinetics of Danusertib binding to Aurora A: three-step kinetics with conformational selection and an induced-fit step

Next, we wanted to shed light on why Danusertib, unlike Gleevec, binds very tightly to Aurora A. A high-resolution X-ray structure shows Danusertib bound to Aurora A's active site with its DFG-loop in the *out* conformation (Figure 5A) (Fancelli et al., 2006), and to rationalize Danusertib's high affinity we measured the kinetics of Danusertib binding to Aurora A directly by stopped-flow experiments at 25 °C. An increase in fluorescence intensity was observed at all Danusertib concentrations and showed double-exponential behavior (Figure 5B). The dependence of the two observed rates constants on drug concentration is linear for one of them (Figure 5C) and non-linear for the other with an apparent plateau at approximately 16 $\pm$ 2 s^{-1} (Figure 5D). The step with linear inhibitor concentration dependence corresponds to the second-order binding step, whereas a non-linear concentration dependency hints at protein conformational transitions. For a hyperbolic increase of the observed rate with substrate concentrations, one cannot *a priori* differentiate between a conformational selection and an induced fit mechanism. However, conformational selection happens before drug binding, and the intrinsic slow DFG-*in* to DFG-*out* interconversion in Aurora A revealed by Gleevec binding (Figure 3A) must, therefore, be unaltered. Since the apparent rate of 16 $\pm$ 2 s^{-1} (Figure 5D) is two orders of magnitude faster, it can only reflect an induced-fit step (i.e., $k_{obs} = k_3 + k_{-3}$).

So, what happened to the conformational selection step? We hypothesize that the lack of this step in our kinetic traces is due to a too small amplitude of this phase, or not observable because of photobleaching having a bigger effect at the longer measurement times. To lessen potential photobleaching, we reduced the enzyme concentration and increased the temperature to 35 °C. Indeed, under these conditions, the slow DFG-*in* to DFG-*out* kinetics were observed as an increase of fluorescence intensity over time with an observed rate constant of approximately 0.1 s^{-1} (Figure 5-*figure supplement 1A*).

While these experiments clearly establish the three-step binding mechanism, it does not provide accurate rate constants for the conformational selection step and it cannot be observed at 25 °C where all the other kinetic experiments are performed. To resolve this issue, we repeated the Aurora A–Gleevec experiment at 25 °C (Figure 5-*figure supplement 2A, B*) and obtained reliable rate constants (k_1 = 0.09 $\pm$ 0.01 s^{-1} and k_{-1} = 0.06 $\pm$ 0.005 s^{-1}) for the conformational selection step in Aurora A, which will be used as "knowns" in what follows. We hypothesize that

the conformational selection step reflects the interconversion between inactive/active conformations and is correlated with the DFG-*out* and -*in* position (Figure 1). The following observations support our hypothesis: (i) two crystal structures for the apo-protein show Trp277 in very different environments (Figure 1E), (ii) Danusertib has been proposed to selectively bind to the DFG-*out* conformation based on a co-crystal structure (Figure 5A) (Fancelli et al., 2006), and (iii) the same slow step is observed for binding of both Gleevec and Danusertib.

Next, the dissociation kinetics for Danusertib was measured by fluorescence and appeared to be extremely slow with an observed slow-off rate of $(3.2 \pm 0.3) \times 10^{-4}$ s^{-1} (Figure 5E). Rationalization of complex binding kinetics cannot be done anymore by visual inspection and kinetic intuition, which can, in fact, be misleading. In order to elucidate the correct binding mechanism and obtain accurate kinetic parameters, all kinetic traces were globally fit (Figure 6) to the three-step binding scheme (Figure 5I). Although global fitting of the binding and dissociation kinetics in KinTek Explorer delivered a value for k_{-2} , evaluation of the kinetic scheme with respect to the time traces exposes that k_{-2} is not well determined from our experiments. We therefore designed a double-jump experiment to populate the $AurA_{out}$:D state followed by dissociation to obtain more accurate information on k_{-2}. Our stopped-flow machine lacks the capability to perform double mixing. Therefore, the double-jump experiment was performed using a Creoptix WAVE instrument. This label-free methodology uses waveguide interferometry to detect refractive index changes due to alteration in surface mass in a vein similar to Surface Plasmon Resonance (SPR). It is an orthogonal technique that sidesteps notable issues associated with fluorescence methods (e.g., photobleaching and inner-filter effects). In short, after immobilizing Aurora A on a WAVEchip, a high concentration of Danusertib was injected for a short, variable period of time, and dissociation was triggered by flowing buffer through the microfluidics channel to remove the drug. The dissociation kinetics fit to a single exponent with a rate constant, k_2, of 6.8 ± 0.4 s^{-1} (Figure 5F and Figure 5-*figure supplement 1B*).

We want to discuss a few additional kinetic features. First, the observed rate constant measured in the dilution experiment (Figure 5E, k_{-3} = $(3.2 \pm 0.3) \times 10^{-4}$ s^{-1}) is slower than k_{-3} from the global fit (k_{-3} = $(7.1 \pm 0.5) \times 10^{-4}$ s^{-1}), which might seem counterintuitive. The observed rate constant was verified by an additional dilution experiment using Creoptix WAVE (k_{-3} = $(2 \pm 0.6) \times 10^{-4}$ s^{-1}, Figure 5-figure supplement 1C). The difference in the observed and microscopic rate constant can, however, be fully reconciled by considering the kinetic partitioning for the proposed scheme, as shown in Figure 6-*figure supplement 1*. Second, a powerful and independent validation of the three-step binding mechanism is obtained by comparing the measured overall K_D of Danusertib with the calculated macroscopic K_D from the microscopic rate

constants (Figure 5G, H, I and Figure 5-*figure supplement 1D*) according to Equation 4, which indeed delivers values that are within experimental error. In addition, our values for k_2, k_{-3}, and K_D are in good agreement with those reported in a recent study using SPR (Willemsen-Seegers et al., 2017).

Our results illuminate trivial but profound principles of binding affinity and lifetime of drug/target complexes: a conformational selection mechanism always weakens the overall inhibitor affinity, while an induced-fit step tightens the affinity depending on how far-shifted the equilibrium in the enzyme/drug complex is (Equations 2, 3 and 4). For DFG-*out* binders (e.g., Danusertib and Gleevec), the DFG-*in* and -*out* equilibrium weakens the overall affinity 1.6-fold; however, the conformational change after drug binding results in a four orders of magnitude tighter binding for Danusertib and is the sole reason for its high affinity to Aurora A compared to Gleevec. The dissociation constants for the bimolecular binding step K_2 is very similar for both inhibitors. Finally, the lifetime of Danusertib on the target is very long because of the very slow conformational dynamics within the Aurora A/Danusertib complex (k_{-3} = (7.1 $\pm$ 0.5) $\times$ 10^{-4} s^{-1}).

Kinetics of AT9283 binding to Aurora A – a surprise

We chose AT9283 as a third inhibitor to characterize the binding mechanism because it has been described as a DFG-*in* binder based on a crystal structure of AT9283 bound to Aurora A (PDB 2W1G, (Howard et al., 2009)). We, therefore, anticipated that in its binding kinetics one can now detect the DFG-*out* to DFG-*in* switch. Rapid kinetic experiments of binding AT9283 to Aurora A at 25 °C resulted in biphasic traces and both processes showed an increase in fluorescence over time (Figure 7A). The k_{obs} for the faster phase (k_2) was linearly dependent on drug concentration reflecting the binding step (Figure 7B) and k_{obs} for the slower phase (k_3) has a limiting value of 0.8 $\pm$ 0.2 s^{-1} and is attributed to an induced-fit step (Figure 7C). For the conformational selection step (i.e., DFG-*out* to DFG-*in*), a decrease in fluorescence is expected because for the reverse flip observed in the Gleevec and Danusertib experiments, a fluorescence increase was seen (Figure 3A and Figure 5-*figure supplement 1A*). However, we could not find any condition (e.g., by varying temperature and ligand concentrations) where such a phase could be observed.

Dissociation is characterized by double-exponential kinetics (Figure 7D and Figure 7-*figure supplement 1A*). The fast phase (~38% of the total amplitude change) decays with a rate constant of (1.1 $\pm$ 0.02) $\times$ 10^{-2} s^{-1}, and the slow phase (~62% of the total change in amplitude) has a rate constant of (0.1 $\pm$ 0.01) $\times$ 10^{-2} s^{-1}. To distinguish between the reverse induced-fit step (k_{-3}) and the physical dissociation step (k_{-2}), a double-jump experiment was performed that unambiguously assigned the faster phase to k_{-2} (Figure 7E and Figure 7-*figure supplement 1B*).

Our attempts to globally fit all kinetic traces assuming binding to only the DFG-*in* state and using the rate constants for the DFG-loop flip from the Gleevec experiment failed (Figure 8-*figure supplement 1A*). An extended model, where AT9283 can bind to both $DFG_{in/out}$ conformations, followed by a common induced-fit step can also not explain the experimental kinetic traces (Figure 8-*figure supplement 1B*). These failures, together with the lack of a detectable conformational selection step, led to a new model in which both the DFG-*in* and DFG-*out* states can bind AT9283, but only $AurA_{in}$:AT can undergo an induced-fit step (Figure 7H). All data can be globally fit to this model (Figure 8) and the overall K_D calculated from the corresponding microscopic rate constants (using Equation 5) is in good agreement with the experimentally measured K_D (Figure 7F-H). Finally, the 10-fold difference between the k_{-3} from the global fit (Figure 7H) and the experimentally observed slow off-rate can be reconciled by kinetic partitioning as shown in Figure 7-*figure supplement 1A.*

Crystal structures of AT9283 bound to Aurora A buttress new binding model

In an effort to structurally verify our model we solved a crystal structure of Aurora A with AT9283 bound and indeed observed the DFG-*out* conformation (PDB 6CPG, Figure 9B and Figure 9-*figure supplement 1*), in contrast to the DFG-*in* conformation as previously reported (Figure 9A) (Howard et al., 2009). Our structure was obtained by co-crystalizing Aurora A with AT9283 and a monobody that binds to the same site as the natural allosteric activator TPX2 (Figure 9B). Binding of this monobody shifts Aurora A into an inactive conformation, with the DFG-loop in the *out* conformation. This new structure underscores the plasticity of Aurora A kinase and the ability of AT9283 to bind to a DFG-*out* state, in addition to the previously reported DFG-*in* state.

Thus, our structural and kinetic data together support that AT9283 can bind to both DFG-*in* and DFG-*out* state of Aurora A, and emphasizes the need for caution when interpreting single X-ray structures.

Inhibitors take advantage of built-in dynamics for ATP binding

We finally compared the binding kinetics of the ATP-competitive inhibitors described above with the natural kinase substrate, ATP (Figure 10). In order to measure stopped-flow kinetics for ATP binding, FRET was measured by exciting Trp residues in Aurora A and detecting fluorescence transfer to the ATP-analogue mant-ATP (Lemaire, Tessmer, Craig, Erie, & Cole, 2006; Ni, Shaffer, & Adams, 2000). The binding of mant-ATP to Aurora A showed biphasic kinetic traces (Figure 10A) that describe the physical binding step (i.e., linear dependence on mant-ATP concentration; Figure 10B) and the induced-fit step (Figure 10C). The observed rate constant

approaches a maximum value defined by the sum of $k_3 + k_{-3}$ (Figure 10C) and the intercept can be estimated to be k_{-3} and is consistent with the value obtained from the k_{off} experiment (Figure 10D). We find that mant-ATP can bind to both the DFG-*in* or -*out* conformations, consistent with our nucleotide-bound crystal structures (Figure 1A-D) and recent single-molecule fluorescence spectroscopy data that indicates that nucleotide binding does not significantly affects this equilibrium (Gilburt et al., 2017). To confirm the model, the kinetic data were globally fit to a two-step binding mechanism (Figure 10H, G). The calculated K_D from the corresponding microscopic rate constants (Figure 10H) is comparable with experimental macroscopic K_D obtained from a titration experiment (Figure 10E, F).

The presence of an induced-fit step for the natural substrate ATP suggests that such conformational change after ligand binding is a built-in property of the enzyme. In other words, inhibitors take advantage of the inherent plasticity of the enzyme that is required for its activity and regulation. The main difference between ATP and inhibitor binding is the rate constant for the reverse induced-fit step (k_{-3}). In the case of ATP, this rate is much faster and, therefore, does not significantly increase the overall affinity. Faster conformational changes and weaker binding are of course prerequisites for efficient turnover; whereas slow conformational changes, particularly the reverse induced-fit step, are at the heart of action for an efficient drug, because it results in tight binding and a long lifetime on the target. In summary, binding of different ligands to the ATP-binding site, such as nucleotides or ATP-competitive inhibitors, is comprised of the physical binding step followed by an induced-fit step. By definition, it is the nature of the induced-fit step that varies for the different ligands since it happens as a result of ligand binding.

Discussion

Characterizing the detailed kinetic mechanisms of drug binding is not just an academic exercise but delivers fundamental knowledge for developing selective inhibitors with high affinity. An induced-fit step turns out to be key for all tight-binding inhibitors studied. From our results on Aurora A kinase presented here and earlier data on Tyrosine-kinases (Agafonov et al., 2014; Wilson et al., 2015), we propose that this is a general mechanism for different kinases and multiple inhibitors, thereby providing a platform for future computational and experimental efforts in rational drug design.

The “use” of a far-shifted induced-fit step for a promising drug is logical for the following reasons: (i) it increases the affinity for the drug by this coupled equilibrium, (ii) it prolongs the residence time of the drug on the target due to the often slow reverse rate, (iii) it is specific for each drug as it happens after the drug binding, and (iv) it can add selectivity for the targets

because it likely involves residues more remote from the active site. An increased drug residence time has significant pharmacological advantages as it can lead to a prolonged biological effect, a decrease of side effects, and a lower risk of metabolic drug modification. Such inhibitors have long been described as slow tight-binding inhibitors (Copeland, 2016; Copeland, Pompliano, & Meek, 2006). The concept of the advantageous roles of induced-fit steps is based on simple thermodynamics and protein flexibility, and is, therefore, likely of relevance for drug design to other targets outside of the kinome.

Additionally, our data provides unique insight into the extensively discussed DFG flip. Combining x-ray crystallography, NMR spectroscopy and stopped-flow kinetics of drug binding establish the nature of this DFG flip both structurally, thermodynamically and kinetically, and resolves the longstanding question of its role for drug affinity and selectivity. Selective binding of a specific DFG-state by Gleevec has been first proposed as the reason for selectivity towards Abl. This conformational selection principle has ever since been at the center of drug discovery for many kinases, including Aurora A (Badrinarayan & Sastry, 2014; Liu & Gray, 2006). Based on our results, we argue that conformational selection of the DFG-state by ATP-competitive inhibitors is a mistakenly pursued concept in drug design for the following reasons: (i) conformational selection by definition weakens the overall ligand affinity, (ii) active site binders are automatically inhibitors, therefore selective binding to a specific DFG-state has no advantage (Badrinarayan & Sastry, 2014; Liu & Gray, 2006), (iii) kinases interconvert between both states. High selectivity gained by DFG-state selective binding could only be achieved in the scenario of a highly skewed population towards the binding-competent state for one kinase relative to all others, which is unfounded.

Our results exemplify why rational drug design is so challenging. The characterization of the complete free-energy landscape of drug binding is needed, which will require more sophisticated computational approaches guided by experimental data such as provided in our study. A good illustration of this point are the computational reports that focused on the DFG flip as a key determinant drug selectivity (Badrinarayan & Sastry, 2014) that now have been ruled out by our kinetic measurements. Our data suggest that future design efforts should be focusing on understanding and exploiting induced-fit steps. The findings presented here are encouraging for developing selective inhibitors even for kinases with very similar folds and drug binding pockets since the action does not happen on a single structural element of the protein but, on a complex energy landscape that is unique to each kinase.

Materials and Methods

Cloning, expression and purification of dephosphorylated Aurora A (122-403) and inhibiting monobody.

Dephosphorylated Aurora A proteins were expressed and purified as described before (Zorba et al., 2014) and analyzed by mass spectrometry to confirm their phosphorylation state. The W227L mutant was generated using the QuickChange Lightning site-directed mutagenesis kit (Agilent).

U-[^{15}N] Aurora A was obtained by growing *E. coli* in M9 minimal medium containing 1 g/L $^{15}NH_4Cl$ (Cambridge Isotope Laboratories, Tewksbury, MA, USA) and 5 g/L D-glucose as the sole nitrogen and carbon source, respectively. [^{15}N]-Trp labeled wild-type Aurora A was obtained using the standard M9 minimal medium, complemented with all amino acids (0.5 g/L) with the exception of tryptophan. One hour prior to induction, 30 mg/L of ^{15}N2-L-Trp (NLM-800; Cambridge Isotope Laboratories, Tewksbury, MA, USA) was added to the medium. Similarly, to obtain samples of wild-type and W277L Aurora A containing 5-fluoro-tryptophan, bacterial growth was performed in unlabeled M9 medium containing all amino acids (0.5 g/L) except for tryptophan. One hour before protein induction, the media was supplemented with 30 mg/L of 5-fluoro-DL-tryptophan (Sigma-Aldrich) (Crowley, Kyne, & Monteith, 2012). NMR samples contained 200-300 µM Aurora A in 50 mM HEPES, pH 7.3, 50 mM NaCl, 20 mM $MgCl_2$, 5 mM TCEP, 2 M TMAO and 10%(v/v) D_2O.

Inhibiting monobody used for co-crystallization with Aurora A and AT9283 was expressed in *E. coli* BL21(DE3) cells harboring the plasmid pHBT containing His_6-tagged-Mb. A culture of TB media containing 50 µg/mL kanamycin that was grown overnight at 37 °C was added to 1L of TB media with 50 µg/mL kanamycin to get a starting OD_{600} of ~0.2. This culture was grown at 37 °C until the OD_{600} reached ~0.8. Protein expression was induced by 0.6 mM IPTG at 18 °C for 13-15 h and cells were harvested by centrifugation. The cell pellet was resuspended in binding buffer (50 mM Tris-HCl, pH 8.0, 300 mM NaCl, 20 mM imidazole, 20 mM $MgCl_2$, 10% glycerol) containing 0.5 mg/mL lysozyme, 5 µg/mL DNase, and 1x EDTA-free protease inhibitor cocktail. Cells were ruptured by sonication on ice then centrifuged at 18,000 rpm at 4 °C for 1 h. The supernatant was loaded onto HisTrap™ HP (GE Healthcare) after filtration using 0.22 µm filtering unit. The pellet was resuspended with GuHCl buffer (20 mM Tris-HCl, pH 8.0, 6 M GuHCl) and allowed to rotate on wheel for 10 min at 4 °C and spun down again. The supernatant was passed through 0.2 µm filtering unit and loaded onto HisTrap™ HP column previously loaded with soluble fraction and pre-equilibrated with GuHCl buffer. Refolding monobody on-column was achieved by washing the HisTrap™ HP column with 5 column volumes (CV) of GuHCl buffer, followed by 5

CV of Triton-X buffer (binding buffer + 0.1% Triton X-100), then 5 CV of β-cyclodextrin buffer (binding buffer + 5 mM β-cyclodextrin), and finally 5 CV of binding buffer. Monobody was eluted with 100% of elution buffer (binding buffer + 500 mM imidazole). The protein was dialyzed overnight in gel-filtration buffer (20 mM Tris-HCl, pH 7.5, 200 mM NaCl, 20 mM $MgCl_2$, 5 mM TCEP, 10% glycerol) in the presence of TEV protease (1:40 TEVP:Mb molar ratio). After dialysis, the TEV-cleaved monobody was passed through HisTrap™ HP column again. The flow-through containing TEV-cleaved monobody was collected and concentrated before loading onto Superdex 200 26/60 gel-filtration column pre-equilibrated with the gel-filtration buffer. The monobody was flash-frozen and stored in -80 °C until use.

X-ray crystallography

Crystals of dephosphorylated (deP) Aurora $A^{122-403}$ + AMPPCP were obtained by mixing 570 μM (18 mg/mL) deP Aurora $A^{122-403}$ and 1 mM AMPPCP in a 2:1 ratio with mother liquor (0.2 M ammonium sulfate, 0.2 M Tris-HCl, pH 7.50, 30% (w/v) PEG-3350). The crystals were grown at 18 °C by vapor diffusion using the hanging-drop method. The protein used for the crystallization was in storage buffer (20 mM Tris-HCl, pH 7.5, 200 mM NaCl, 10% (v/v) glycerol, 20 mM $MgCl_2$, 1 mM TCEP); AMPPCP was freshly prepared before use in the same buffer. Crystals were flash-frozen in liquid nitrogen prior to shipping. Crystals of apo, deP Aurora $A^{122-403}$ were grown at 18 °C by vapor diffusion using the sitting-drop method (96-well plate). A 1:1 ratio of protein to mother liquor was obtained by combining 0.5 μL of 300 μM (10 mg/mL) deP Aurora $A^{122-403}$ in 50 mM HEPES, pH 7.3, 500 mM ammonium acetate, 1 mM $MgCl_2$, 5 mM TCEP) with 0.5 μL of 0.15 M Tris-HCl, pH 7.5, 0.15 M ammonium sulfate, 35% (w/v) PEG-3350. Crystals were soaked for 10-20 s in cryo buffer (20% (w/v) PEG-400, 20% ethylene glycol, 10% water and 50% mother liquor) before flash-freezing in liquid nitrogen. The complex between Aurora $A^{122-403}$, inhibiting monobody (Mb) and AT9283 was crystallized at 18 °C by vapor diffusion using the sitting-drop method. In short, a 1:1 ratio of protein mixture to mother liquor was obtained by combining 0.5 μL of sample [240 μM deP Aurora $A^{122-403}$ + 1.0 mM AT9283 + 250 μM Mb] with 0.5 μL of mother liquor [0.1 M Bis-Tris, pH 5.5, 0.2 M magnesium chloride, 19% (w/v) PEG-3350]. Crystals were soaked for 10-20 s in cryo buffer (17.5% (w/v) PEG-400, 17.5% ethylene glycol, 45% water and 20% mother liquor) before flash-freezing in liquid nitrogen.

Diffraction data were collected at 100 K at the Advanced Light Source (Lawrence Berkeley National Laboratory) beamlines ALS 8.2.1 (apo-AurA and AurA+Mb+AT9283) and 8.2.2 (AurA+AMPPCP) with a collection wavelength of 1.00 Å.

Data were indexed and integrated using iMOSFLM (Battye, Kontogiannis, Johnson,

Powell, & Leslie, 2011) for apo/AMPPCP-bound Aurora A and Xia2 (Winter, 2010) using XDS (Kabsch, 2010) for the Aurora A/Mb/AT9283 complex, respectively. Data were scaled and merged with AIMLESS (Evans & Murshudov, 2013), in the case of Aurora A/Mb/AT9283 two data separate data sets were merged. All software was used within the CCP4 software suite (Winn et al., 2011).

As initial search models 1MQ4 (Nowakowski et al., 2002) and 3K2M (Wojcik et al., 2010) were used for Aurora A and monobody, respectively, and molecular replacement was performed using Phaser (McCoy et al., 2007). The molecules were placed in the unit cell using the ACHESYM webserver (Kowiel, Jaskolski, & Dauter, 2014). Iterative refinements were carried out with PHENIX (Adams et al., 2010), using rosetta.refine (DiMaio et al., 2013) and phenix.refine (Afonine et al., 2012), and manual rebuilding was performed in Coot (Emsley & Cowtan, 2004; Emsley, Lohkamp, Scott, & Cowtan, 2010).

Structure validation was performed using MolProbity (V. B. Chen et al., 2010) and yielded the statistics given below. The Ramachandran statistics for dephosphorylated apo (AMPPCP-bound) Aurora A are: favored: 93.65 (94.90)%, allowed 5.95 (4.71)%, outliers: 0.4 (0.39)%); 0.48 (0.0)% rotamer outliers and an all-atom clashscore of 4.45 (2.44). For the Aurora A/Mb/AT9283 complex, the Ramachandran statistics are: favored: 92.64%, allowed 7.06%, outliers: 0.3%); 0.0 % rotamer outliers and an all-atom clashscore of 2.81. We note that the B-factors for the monobodies in the complex of Aurora A/Mb/AT9283 are rather high, indicating significantly flexibility in the parts that are not part of the binding interface with Aurora A.

The data collection and refinement statistics are given in Figure 1-*figure supplement 1* and Figure 9-*figure supplement 1*. Structure factors and refined models have been deposited in the PDB under accession codes: 6CPE (apo Aurora A), 6CPF (Aurora A + AMPPCP) and 6CPG (Aurora A/Mb/AT9283).

All figures were generated using Chimera (Pettersen et al., 2004).

NMR spectroscopy

All ^{19}F NMR experiments were performed at 35 °C on a Varian Unity Inova 500 MHz spectrometer, equipped with a ^{1}H/^{19}F switchable probe tuned to fluorine (90° pulse width of 12 µs). All 1D ^{19}F spectra were recorded with a spectral width of ~60 ppm and a maximum evolution time of 0.25 s. An interscan delay of 1.5 s was used with 5,000 scans per transients, giving rise to a total acquisition time of 2.5 h per spectrum. To remove background signal from the probe and avoid baseline distortions, data acquisition was started after a ~100 µs delay (using the "delacq" macro) and appropriate shifting of the data followed by backward linear prediction was performed. The

data were apodized with an exponential filter (2.5 Hz line broadening) and zero-filled before Fourier transform. To improve the signal-to-noise ratio several data sets were recorded consecutively and, provided that the sample remained stable, added together after processing (two for apo Aurora A, four for Aurora A + AMPPCP, and five for W277L + AMPPCP, respectively). ^{19}F chemical shifts were referenced externally to trifluoroacetic acid (TFA) at -76.55 ppm.

[^{1}H-^{15}N]-TROSY-HSQC experiments were recorded at 25 °C on an Agilent DD2 600 MHz four-channel spectrometer equipped with a triple-resonance cryogenically cooled probe-head. Typically, 115–128 (^{15}N) × 512 (^{1}H) complex points, with maximum evolution times equal to 48.5–64 (^{15}N) × 64 (^{1}H) ms. An interscan delay of 1.0 s was used along with 32 or 56 scans per transient, giving rise to a net acquisition time 1.5-2.5 h for each experiment. To improve the signal-to-noise ratio several data sets were recorded consecutively and, provided that the sample remained stable, added together after processing (typically three data sets per sample).

All data sets were processed with the NMRPipe/NMRDraw software package (Delaglio et al., 1995) and 2D spectra were visualized using Sparky (Goddard, 2008). Deconvolution of the ^{19}F spectra and line shape fitting was performed using the Python package nmrglue (Helmus & Jaroniec, 2013).

Kinetics experiments of Aurora A with Gleevec, Danusertib, and AT9283

Stopped-flow experiment. Intrinsic tryptophan fluorescence spectroscopy was used to monitor drug binding kinetics to Aurora A. All experiments were performed at 25 °C, except for the Gleevec kinetics that were measured at 10 °C (unless otherwise stated) because the binding of Gleevec to Aurora A is too fast $k_{obs,Binding}$. Stock solutions of 200 mM Danusertib, 200 mM AT9283 and 50 mM Gleevec (all purchased from Selleck Chemicals) were prepared in 100% DMSO were and stored at -80 °C until used. Aurora A used in the kinetic experiments was dephosphorylated Aurora A as determined by mass spectrometry, Western blot and activity experiments (data not shown). The rapid kinetics were studied using a stopped-flow spectrophotometer (SX20 series from Applied Photophysics Ltd). The flow system was made anaerobic by rinsing with degassed buffer comprised of 50 mM HEPES, 50 mM NaCl, 20 mM $MgCl_2$, 5 mM TCEP, 5% DMSO, pH 7.30 to minimize photobleaching. The stock solutions of Aurora A and all drugs were made anaerobic by degassing with ThermoVac (MicroCal) at the desired temperature. In general, a solution of 5 μM Aurora A was loaded in one syringe and quickly mixed with drug, prepared in the same buffer, in the other syringe (mixing ratio 1:10). A significant increase or decrease in the fluorescence intensity of Aurora A (excitation at 295 nm, emission cut-off at 320 nm) can be observed due to the drug binding. For each drug concentration, at least five replicate

measurements were made and these transients were averaged. Analysis was performed by fitting the individual trace to exponential equations using Pro-Data Viewer (Applied Photophysics Ltd) or with Kinesyst 3 software (TgK Scientific) and error bars denote the standard errors as obtained from the fit. KaleidaGraph version 4.5.3 (Synergy) was used for data analysis and plotting. All kinetic data were globally fitted in KinTek Explorer software (Johnson, 2009; Johnson, Simpson, & Blom, 2009).

Under the rapid equilibrium approximation, the binding and dissociation steps of Gleevec to Aurora A are fast compared to conformational selection, therefore the value of k_1 and k_{-1} can be estimated according to Equation 1:

$$k_{obs} = \frac{k_{-1}}{1+\left(\frac{[Gleevec]}{[Aurora\ A]+\left(\frac{k_{-2}}{k_2}\right)}\right)} + k_1 \qquad \text{Equation 1}$$

where k_1 and k_{-1}represent the conformational change from DFG-*in* to -*out* and vice versa, respectively. The approximate values of k_1 and k_{-1} obtained from fitting to this equation are used as starting values for the global fit.

For the 5 μM Aurora A/Gleevec complex, the release of the drug was recorded after a 11-fold dilution of the complex using the stopped-flow instrument for 0.25 s (excitation at 295 nm, emission cut-off at 320 nm) at 10 °C.

Creoptix WAVE experiments. Double jump, slow-off, and macroscopic K_D experiments of Aurora A with drugs were studied using a Creoptix WAVE instrument (Creoptix AG, Wädenswil, Switzerland) at 25 °C. All chemicals were purchased from GE Healthcare, unless otherwise stated. The protocols in the WAVEcontrol software for conditioning of the chip, immobilization of proteins and performing kinetics experiments were followed. In short, the polycarboxylate chip (PCH) was activated by injection of a 1:1 mixture with final concentrations of 200 mM N-ethyl-N'-(3-dimethylaminopropyl)carbodiimide (EDC) and 50 mM N-hydroxysuccinimide (NHS), followed by streptavidin immobilization (50 μg/mL in 10 mM sodium acetate pH 5.0). Unreacted sites on the chip were blocked with 1 M ethanolamine pH 8.0. For all activation, immobilization and passivation steps 0.2x HBS-EP was used as running buffer with a flowrate of 10 μL/min and an injection duration of 420 s on both channels 1 and 2.

Biotinylated T288V variant that mimics dephosphorylated Aurora A was used for experiments performed on the Creoptix WAVE instrument. The activity of T288V with substrate

Lats2, the macroscopic K_D and slow-off rate of Danusertib were the same as wild-type (data not shown). Biotinylated T288V Aurora A (70 μg/mL) was immobilized on the PCH-streptavidin chip with 10 μL/min injection and 15 s injection duration over channel 1 only (channel 2 was used as reference channel). All experiments were run in 50 mM HEPES, 50 mM NaCl, 20 mM $MgCl_2$, 5 mM TCEP, 0.03 mg/mL BSA, 0.005% Tween-20, pH 7.30 as running buffer. Binding experiments were evaluated over a range of Danusertib (0.13 – 66.67 nM), AT9283 (0.03 – 64.8 nM), and Gleevec (0.37 – 40 μM) concentrations. Gleevec binding experiments contained 5% DMSO in the running buffer (see above) to enhance Gleevec's solubility. Double-jump experiments of Aurora A/drugs were performed by injecting 1 μM Danusertib or AT9283 with 0.2, 0.4, 0.8, and 2 s injection duration for Danusertib and 1 and 3 s injection duration for AT9283 followed by a 60 s dissociation duration per injection. The slow-off experiments were performed by injecting 5 μM Danusertib or AT9283 with 5-10 s injection duration (to fully saturate Aurora A) followed by a 180 s injection of buffer to remove the excess drug and the dissociation was measured for a duration of 10800 s.

Spectrofluorometer experiments. The spectrofluorometer FluoroMax-4 (Horiba Scientific) with temperature controller was used to study the slow-off rate of Aurora A with Danusertib at 25 °C. For this experiment, a solution containing 30 nM Aurora A and 30 nM Danusertib was pre-incubated for an hour, before diluting 30-fold into degassed buffer (ratio 1:30). A significant decrease in the fluorescence intensity of Aurora A (excitation at 295 nm, emission at 340 nm) can be seen due to the Danusertib release. The fluorescence signal was recorded every 160 s for a duration of six hours using the photobleaching minimization option that will close the shutter after each acquisition. A control experiment was performed, using the same experimental conditions, but without drug in order to account for photobleaching.

Overall dissociation constant calculated from intrinsic rate constants. In the following equations, K_1, K_2, K_3 and K_4 equal to:

$$K_1 = \frac{k_{-1}}{k_1}$$

$$K_2 = \frac{k_{-2}}{k_2} = \frac{k_{off}}{k_{on}}$$

$$K_3 = \frac{k_{-3}}{k_3}$$

$$K_4 = \frac{k_{-4}}{k_4}$$

606 Conformational selection followed by inhibitor binding:

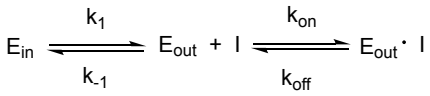

607 K_1 K_2 $K_D = (K_1 + 1)*K_2$ Equation 2

608

609 Inhibitor binding followed by an induced-fit step:

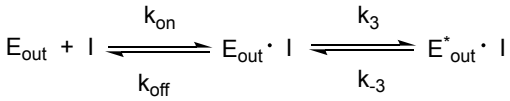

K_2 K_3 $K_D = \frac{K_2*K_3}{(K_3 + 1)}$

610 Equation 3

611

612 Conformational selection followed by inhibitor binding and an induced-fit step:

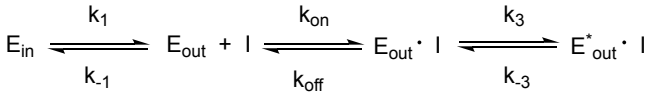

K_1 K_2 K_3 $K_D = \frac{(K_1 + 1)*K_2*K_3}{(K_3 + 1)}$

613 Equation 4

614

615 Conformational selection mechanism, followed by inhibitor binding to both DFG-*in* and -*out* state,
616 but an induced-fit step only occurs in the DFG-*in* state:

617

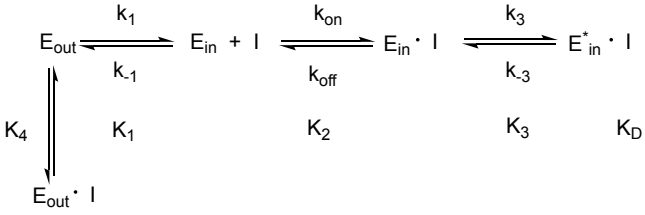

$K_D = \frac{(K_1 + 1)*K_2*K_3*K_4}{K_1*K_2*K_3 + K_3*K_4 + K_4}$

618 Equation 5

619

620 The uncertainties in the calculated dissociation constant parameter using the equations above
621 are obtained using standard error propagation.

622

623 **Aurora A binding to mant-ATP**. FRET using intrinsic tryptophan fluorescence is used to monitor
624 mant-ATP binding kinetics to Aurora A at 10 °C. In the binding experiment or k_{on}, increasing
625 concentration of mant-ATP were quickly mixed to 0.5 μM Aurora A (ratio 1:10, excitation at 295
626 nm, emission cut-off at 395 nm). In the experiment to measure the release of mant-ATP or k_{off},

10 μM/10 μM Aurora A/mant-ATP complex was diluted with buffer (ratio 1:10). A significant decrease in the fluorescence intensity of Aurora A (excitation at 295 nm, emission cut-off at 395 nm) can be seen due to the mant-ATP release.

Macroscopic dissociation constant experiments

Fluorescence titration experiments were measured using FluoroMax-4 spectrofluorometer (Horiba Scientific). Increasing amounts of Aurora A/Danusertib complex (4 nM Aurora A and 150 nM Danusertib) or Aurora A/mant-ATP (1 μM Aurora A and 2 mM mant-ATP) were titrated into an Aurora A solution (4 nM and 1 μM Aurora A for experiments with Danusertib and mant-ATP, respectively). To measure Danusertib affinity, the excitation wavelength was 295 nm (5 nm bandwidth) and emission spectra were recorded from 310–450 nm (20 nm bandwidth) in increments of 2 nm and the temperature was maintained at 25 °C. For the mant-ATP experiment, the dissociation constant was measured at 10 °C using fluorescence energy transfer from tryptophan residues in Aurora A to mant-ATP by setting the excitation wavelength to 290 nm (5 nm bandwidth) and collecting the emission intensity from 310–550 nm (5 nm bandwidth) in increments of 2 nm. A control experiment in the absence of Aurora A was performed using the same experimental settings and used to correct for the mant-ATP interference. In all experiments, a 5 minutes equilibration time was used after each addition of Aurora A/Danusertib complex or Aurora A/mant-ATP complex.

The fluorescence intensity at 368 nm versus Danusertib concentration or the change in fluorescence at 450 nm (ΔF^{450}) versus mant-ATP concentration was fitted to Equation 6 using Marquardt-Levenberg nonlinear fitting algorithm included in KaleidaGraph to obtain the K_D.

$$\mathrm{F} = \mathrm{F}_0 + \mathrm{A} \cdot \frac{[\mathrm{I}]+[E_t]+K_D-\sqrt{([\mathrm{I}]+[E_t]+K_D)^2-4\cdot[E_t]\cdot[\mathrm{I}])}}{2\cdot[E_t]} \qquad \text{Equation 6}$$

F and F_0 are the fluorescence and initial fluorescence intensities, respectively. [I] and $[E_t]$ are the total concentration of the drug or mant-ATP and the Aurora A, respectively.

Acknowledgments

We thank C. Sassetti (University of Massachusetts Medical School, Worcester) for the use of the ESI-Q-TOF instrument, and the Advanced Light Source (ALS), Berkeley, CA, USA, for access to beamlines BL8.2.1. and BL8.2.2. The Berkeley Center for Structural Biology is supported in part by the National Institutes of Health, National Institute of General Medical Sciences, and the HHMI.

The ALS is supported by the Director, Office of Science, Office of Basic Energy Sciences, of the U.S. Department of Energy under contract DE-AC02-05CH11231. We thank Shohei and Akiko Koide (New York University) for the plasmid of the monody used here. This work was supported by the Howard Hughes Medical Institute (HHMI); the Office of Basic Energy Sciences, Catalysis Science Program, U.S. Dept. of Energy (award DE-FG02-05ER15699); and the NIH (grant GM100966-01). R.O. was a HHMI Fellow of the Damon Runyon Cancer Research Foundation (DRG-2114-12).

Competing interests

All authors declare no competing financial or other interests.

References

Adams, P. D., Afonine, P. V., Bunkoczi, G., Chen, V. B., Davis, I. W., Echols, N., . . . Zwart, P. H. (2010). PHENIX: a comprehensive Python-based system for macromolecular structure solution. *Acta Crystallogr D Biol Crystallogr, 66*(Pt 2), 213-221. doi:10.1107/S0907444909052925

Afonine, P. V., Grosse-Kunstleve, R. W., Echols, N., Headd, J. J., Moriarty, N. W., Mustyakimov, M., . . . Adams, P. D. (2012). Towards automated crystallographic structure refinement with phenix.refine. *Acta Crystallogr D Biol Crystallogr, 68*(Pt 4), 352-367. doi:10.1107/S0907444912001308

Agafonov, R. V., Wilson, C., Otten, R., Buosi, V., & Kern, D. (2014). Energetic dissection of Gleevec's selectivity toward human tyrosine kinases. *Nat Struct Mol Biol, 21*(10), 848-853. doi:10.1038/nsmb.2891

Asteriti, I. A., Daidone, F., Colotti, G., Rinaldo, S., Lavia, P., Guarguaglini, G., & Paiardini, A. (2017). Identification of small molecule inhibitors of the Aurora-A/TPX2 complex. *Oncotarget, 8*(19), 32117-32133. doi:10.18632/oncotarget.16738

Badrinarayan, P., & Sastry, G. N. (2014). Specificity rendering 'hot-spots' for aurora kinase inhibitor design: the role of non-covalent interactions and conformational transitions. *PLoS One, 9*(12), e113773. doi:10.1371/journal.pone.0113773

Barakat, K. H., Huzil, J. T., Jordan, K. E., Evangelinos, C., Houghton, M., & Tuszynski, J. (2013). A computational model for overcoming drug resistance using selective dual-inhibitors for aurora kinase A and its T217D variant. *Mol Pharm, 10*(12), 4572-4589. doi:10.1021/mp4003893

Battye, T. G., Kontogiannis, L., Johnson, O., Powell, H. R., & Leslie, A. G. (2011). iMOSFLM: a new graphical interface for diffraction-image processing with MOSFLM. *Acta Crystallogr D Biol Crystallogr, 67*(Pt 4), 271-281. doi:10.1107/S0907444910048675

Bavetsias, V., & Linardopoulos, S. (2015). Aurora Kinase Inhibitors: Current Status and Outlook. *Front Oncol, 5*, 278. doi:10.3389/fonc.2015.00278

Bavetsias, V., Perez-Fuertes, Y., McIntyre, P. J., Atrash, B., Kosmopoulou, M., O'Fee, L., . . . Blagg, J. (2015). 7-(Pyrazol-4-yl)-3H-imidazo[4,5-b]pyridine-based derivatives for kinase inhibition: Co-crystallisation studies with Aurora-A reveal distinct differences in the orientation of the pyrazole N1-substituent. *Bioorg Med Chem Lett, 25*(19), 4203-4209. doi:10.1016/j.bmcl.2015.08.003

Bayliss, R., Burgess, S. G., & McIntyre, P. J. (2017). Switching Aurora-A kinase on and off at an allosteric site. *FEBS J, 284*(18), 2947-2954. doi:10.1111/febs.14069

Bayliss, R., Sardon, T., Vernos, I., & Conti, E. (2003). Structural basis of Aurora-A activation by TPX2 at the mitotic spindle. *Molecular Cell, 12*(4), 851-862. doi:Doi 10.1016/S1097-2765(03)00392-7

Borisa, A. C., & Bhatt, H. G. (2017). A comprehensive review on Aurora kinase: Small molecule inhibitors and clinical trial studies. *Eur J Med Chem, 140*, 1-19. doi:10.1016/j.ejmech.2017.08.045

Burgess, S. G., Oleksy, A., Cavazza, T., Richards, M. W., Vernos, I., Matthews, D., & Bayliss, R. (2016). Allosteric inhibition of Aurora-A kinase by a synthetic vNAR domain. *Open Biol, 6*(7). doi:10.1098/rsob.160089

Campos-Olivas, R., Marenchino, M., Scapozza, L., & Gervasio, F. L. (2011). Backbone assignment of the tyrosine kinase Src catalytic domain in complex with imatinib. *Biomol NMR Assign, 5*(2), 221-224. doi:10.1007/s12104-011-9304-7

Carpinelli, P., Ceruti, R., Giorgini, M. L., Cappella, P., Gianellini, L., Croci, V., . . . Moll, J. (2007). PHA-739358, a potent inhibitor of Aurora kinases with a selective target inhibition profile relevant to cancer. *Mol Cancer Ther, 6*(12 Pt 1), 3158-3168. doi:10.1158/1535-7163.MCT-07-0444

Carvajal, R. D., Tse, A., & Schwartz, G. K. (2006). Aurora kinases: new targets for cancer therapy. *Clin Cancer Res, 12*(23), 6869-6875. doi:10.1158/1078-0432.CCR-06-1405

Cheetham, G. M., Knegtel, R. M., Coll, J. T., Renwick, S. B., Swenson, L., Weber, P., . . . Austen, D. A. (2002). Crystal structure of aurora-2, an oncogenic serine/threonine kinase. *J Biol Chem, 277*(45), 42419-42422. doi:10.1074/jbc.C200426200

Chen, C., Ha, B. H., Thevenin, A. F., Lou, H. J., Zhang, R., Yip, K. Y., . . . Turk, B. E. (2014). Identification of a major determinant for serine-threonine kinase phosphoacceptor specificity. *Molecular Cell, 53*(1), 140-147. doi:10.1016/j.molcel.2013.11.013

Chen, V. B., Arendall, W. B., 3rd, Headd, J. J., Keedy, D. A., Immormino, R. M., Kapral, G. J., . . . Richardson, D. C. (2010). MolProbity: all-atom structure validation for macromolecular crystallography. *Acta Crystallogr D Biol Crystallogr, 66*(Pt 1), 12-21. doi:10.1107/S0907444909042073

Cohen, P. (2002). Protein kinases - the major drug targets of the twenty-first century? *Nature Reviews Drug Discovery, 1*(4), 309-315. doi:10.1038/nrd773

Copeland, R. A. (2016). The drug-target residence time model: a 10-year retrospective. *Nature Reviews Drug Discovery, 15*(2), 87-95. doi:10.1038/nrd.2015.18

Copeland, R. A., Pompliano, D. L., & Meek, T. D. (2006). Drug-target residence time and its implications for lead optimization. *Nature Reviews Drug Discovery, 5*(9), 730-739. doi:10.1038/nrd2082

Crowley, P. B., Kyne, C., & Monteith, W. B. (2012). Simple and inexpensive incorporation of 19F-tryptophan for protein NMR spectroscopy. *Chem Commun (Camb), 48*(86), 10681-10683. doi:10.1039/c2cc35347d

Delaglio, F., Grzesiek, S., Vuister, G. W., Zhu, G., Pfeifer, J., & Bax, A. (1995). NMRPipe: a multidimensional spectral processing system based on UNIX pipes. *J Biomol NMR, 6*(3), 277-293.

DiMaio, F., Echols, N., Headd, J. J., Terwilliger, T. C., Adams, P. D., & Baker, D. (2013). Improved low-resolution crystallographic refinement with Phenix and Rosetta. *Nat Methods, 10*(11), 1102-1104. doi:10.1038/nmeth.2648

Dodson, C. A., Kosmopoulou, M., Richards, M. W., Atrash, B., Bavetsias, V., Blagg, J., & Bayliss, R. (2010). Crystal structure of an Aurora-A mutant that mimics Aurora-B bound to MLN8054: insights into selectivity and drug design. *Biochemical Journal, 427*, 19-28. doi:10.1042/Bj20091530

Emsley, P., & Cowtan, K. (2004). Coot: model-building tools for molecular graphics. *Acta Crystallogr D Biol Crystallogr, 60*(Pt 12 Pt 1), 2126-2132. doi:10.1107/S0907444904019158

Emsley, P., Lohkamp, B., Scott, W. G., & Cowtan, K. (2010). Features and development of Coot. *Acta Crystallogr D Biol Crystallogr, 66*(Pt 4), 486-501. doi:10.1107/S0907444910007493

Evans, P. R., & Murshudov, G. N. (2013). How good are my data and what is the resolution? *Acta Crystallogr D Biol Crystallogr, 69*(Pt 7), 1204-1214. doi:10.1107/S0907444913000061

Fancelli, D., Moll, J., Varasi, M., Bravo, R., Artico, R., Berta, D., . . . Vianello, P. (2006). 1,4,5,6-tetrahydropyrrolo[3,4-c]pyrazoles: identification of a potent Aurora kinase inhibitor with a favorable antitumor kinase inhibition profile. *J Med Chem, 49*(24), 7247-7251. doi:10.1021/jm060897w

Ferguson, F. M., Doctor, Z. M., Chaikuad, A., Sim, T., Kim, N. D., Knapp, S., & Gray, N. S. (2017). Characterization of a highly selective inhibitor of the Aurora kinases. *Bioorg Med Chem Lett, 27*(18), 4405-4408. doi:10.1016/j.bmcl.2017.08.016

Fraedrich, K., Schrader, J., Ittrich, H., Keller, G., Gontarewicz, A., Matzat, V., . . . Benten, D. (2012). Targeting Aurora Kinases with Danusertib (PHA-739358) Inhibits Growth of Liver Metastases from Gastroenteropancreatic Neuroendocrine Tumors in an Orthotopic Xenograft Model. *Clinical Cancer Research, 18*(17), 4621-4632. doi:10.1158/1078-0432.Ccr-11-2968

Fu, J. Y., Bian, M. L., Jiang, Q., & Zhang, C. M. (2007). Roles of aurora kinases in mitosis and tumorigenesis. *Molecular Cancer Research, 5*(1), 1-10. doi:10.1158/1541-7786.Mcr-06-0208

Gautschi, O., Heighway, J., Mack, P. C., Purnell, P. R., Lara, P. N., & Gandara, D. R. (2008). Aurora kinases as anticancer drug targets. *Clinical Cancer Research, 14*(6), 1639-1648. doi:10.1158/1078-0432.Ccr-07-2179

Gilburt, J. A. H., Sarkar, H., Sheldrake, P., Blagg, J., Ying, L., & Dodson, C. A. (2017). Dynamic Equilibrium of the Aurora A Kinase Activation Loop Revealed by Single-Molecule Spectroscopy. *Angew Chem Int Ed Engl, 56*(38), 11409-11414. doi:10.1002/anie.201704654

Goddard, T. D. K., D.G. (2008). SPARKY 3 (Version 3.115). San Francisco: University of California.

Helmus, J. J., & Jaroniec, C. P. (2013). Nmrglue: an open source Python package for the analysis of multidimensional NMR data. *J Biomol NMR, 55*(4), 355-367. doi:10.1007/s10858-013-9718-x

Heron, N. M., Anderson, M., Blowers, D. P., Breed, J., Eden, J. M., Green, S., . . . Rowsell, S. (2006). SAR and inhibitor complex structure determination of a novel class of potent and specific Aurora kinase inhibitors. *Bioorg Med Chem Lett, 16*(5), 1320-1323. doi:10.1016/j.bmcl.2005.11.053

Hopkins, A. L., & Groom, C. R. (2002). The druggable genome. *Nature Reviews Drug Discovery, 1*(9), 727-730. doi:10.1038/nrd892

Howard, S., Berdini, V., Boulstridge, J. A., Carr, M. G., Cross, D. M., Curry, J., . . . Wyatt, P. G. (2009). Fragment-based discovery of the pyrazol-4-yl urea (AT9283), a multitargeted kinase inhibitor with potent aurora kinase activity. *J Med Chem, 52*(2), 379-388. doi:10.1021/jm800984v

Iqbal, N., & Iqbal, N. (2014). Imatinib: a breakthrough of targeted therapy in cancer. *Chemother Res Pract, 2014*, 357027. doi:10.1155/2014/357027

Janecek, M., Rossmann, M., Sharma, P., Emery, A., Huggins, D. J., Stockwell, S. R., . . . Venkitaraman, A. R. (2016). Allosteric modulation of AURKA kinase activity by a small-molecule inhibitor of its protein-protein interaction with TPX2. *Sci Rep, 6*, 28528. doi:10.1038/srep28528

Johnson, K. A. (2009). Fitting enzyme kinetic data with KinTek Global Kinetic Explorer. *Methods Enzymol, 467*, 601-626. doi:10.1016/S0076-6879(09)67023-3

Johnson, K. A., Simpson, Z. B., & Blom, T. (2009). Global Kinetic Explorer: A new computer program for dynamic simulation and fitting of kinetic data. *Analytical Biochemistry, 387*(1), 20-29. doi:10.1016/j.ab.2008.12.024

Kabsch, W. (2010). Xds. *Acta Crystallogr D Biol Crystallogr, 66*(Pt 2), 125-132. doi:10.1107/S0907444909047337

Katayama, H., & Sen, S. (2010). Aurora kinase inhibitors as anticancer molecules. *Biochimica Et Biophysica Acta-Gene Regulatory Mechanisms, 1799*(10-12), 829-839. doi:10.1016/j.bbagrm.2010.09.004

Kilchmann, F., Marcaida, M. J., Kotak, S., Schick, T., Boss, S. D., Awale, M., . . . Reymond, J. L. (2016). Discovery of a Selective Aurora A Kinase Inhibitor by Virtual Screening. *J Med Chem, 59*(15), 7188-7211. doi:10.1021/acs.jmedchem.6b00709

Kitevski-LeBlanc, J. L., & Prosser, R. S. (2012). Current applications of 19F NMR to studies of protein structure and dynamics. *Prog Nucl Magn Reson Spectrosc, 62*, 1-33. doi:10.1016/j.pnmrs.2011.06.003

Kollareddy, M., Zheleva, D., Dzubak, P., Brahmkshatriya, P. S., Lepsik, M., & Hajduch, M. (2012). Aurora kinase inhibitors: progress towards the clinic. *Invest New Drugs, 30*(6), 2411-2432. doi:10.1007/s10637-012-9798-6

Kornev, A. P., & Taylor, S. S. (2010). Defining the conserved internal architecture of a protein kinase. *Biochimica Et Biophysica Acta-Proteins and Proteomics, 1804*(3), 440-444. doi:10.1016/j.bbapap.2009.10.017

Kornev, A. P., & Taylor, S. S. (2015). Dynamics-Driven Allostery in Protein Kinases. *Trends Biochem Sci, 40*(11), 628-647. doi:10.1016/j.tibs.2015.09.002

Kowiel, M., Jaskolski, M., & Dauter, Z. (2014). ACHESYM: an algorithm and server for standardized placement of macromolecular models in the unit cell. *Acta Crystallogr D Biol Crystallogr, 70*(Pt 12), 3290-3298. doi:10.1107/S1399004714024572

Langer, T., Vogtherr, M., Elshorst, B., Betz, M., Schieborr, U., Saxena, K., & Schwalbe, H. (2004). NMR backbone assignment of a protein kinase catalytic domain by a combination of

837 several approaches: application to the catalytic subunit of cAMP-dependent protein
838 kinase. *Chembiochem, 5*(11), 1508-1516. doi:10.1002/cbic.200400129
839 Lemaire, P. A., Tessmer, I., Craig, R., Erie, D. A., & Cole, J. L. (2006). Unactivated PKR exists in
840 an open conformation capable of binding nucleotides. *Biochemistry, 45*(30), 9074-
841 9084. doi:10.1021/bi060567d
842 Liu, Y., & Gray, N. S. (2006). Rational design of inhibitors that bind to inactive kinase
843 conformations. *Nat Chem Biol, 2*(7), 358-364. doi:10.1038/nchembio799
844 Lok, W., Klein, R. Q., & Saif, M. W. (2010). Aurora kinase inhibitors as anti-cancer therapy.
845 *Anticancer Drugs, 21*(4), 339-350. doi:10.1097/CAD.0b013e3283350dd1
846 Lovera, S., Sutto, L., Boubeva, R., Scapozza, L., Dolker, N., & Gervasio, F. L. (2012). The different
847 flexibility of c-Src and c-Abl kinases regulates the accessibility of a druggable inactive
848 conformation. *J Am Chem Soc, 134*(5), 2496-2499. doi:10.1021/ja210751t
849 Lukasiewicz, K. B., & Lingle, W. L. (2009). Aurora A, centrosome structure, and the
850 centrosome cycle. *Environ Mol Mutagen, 50*(8), 602-619. doi:10.1002/em.20533
851 Martin, M. P., Zhu, J. Y., Lawrence, H. R., Pireddu, R., Luo, Y., Alam, R., . . . Schonbrunn, E. (2012).
852 A novel mechanism by which small molecule inhibitors induce the DFG flip in Aurora
853 A. *ACS Chem Biol, 7*(4), 698-706. doi:10.1021/cb200508b
854 Marumoto, T., Zhang, D. W., & Saya, H. (2005). Aurora-A - A guardian of poles. *Nature Reviews*
855 *Cancer, 5*(1), 42-50. doi:10.1038/nrc1526
856 Marzo, I., & Naval, J. (2013). Antimitotic drugs in cancer chemotherapy: Promises and pitfalls.
857 *Biochemical Pharmacology, 86*(6), 703-710. doi:10.1016/j.bcp.2013.07.010
858 McCoy, A. J., Grosse-Kunstleve, R. W., Adams, P. D., Winn, M. D., Storoni, L. C., & Read, R. J.
859 (2007). Phaser crystallographic software. *Journal of Applied Crystallography, 40*(Pt 4),
860 658-674. doi:10.1107/S0021889807021206
861 McIntyre, P. J., Collins, P. M., Vrzal, L., Birchall, K., Arnold, L. H., Mpamhanga, C., . . . Bayliss, R.
862 (2017). Characterization of Three Druggable Hot-Spots in the Aurora-A/TPX2
863 Interaction Using Biochemical, Biophysical, and Fragment-Based Approaches. *ACS*
864 *Chem Biol, 12*(11), 2906-2914. doi:10.1021/acschembio.7b00537
865 Meng, Y., Lin, Y. L., & Roux, B. (2015). Computational study of the "DFG-flip" conformational
866 transition in c-Abl and c-Src tyrosine kinases. *J Phys Chem B, 119*(4), 1443-1456.
867 doi:10.1021/jp511792a
868 Nagar, B., Bornmann, W. G., Pellicena, P., Schindler, T., Veach, D. R., Miller, W. T., . . . Kuriyan,
869 J. (2002). Crystal structures of the kinase domain of c-Abl in complex with the small
870 molecule inhibitors PD173955 and imatinib (STI-571). *Cancer Res, 62*(15), 4236-
871 4243.
872 Ni, Q., Shaffer, J., & Adams, J. A. (2000). Insights into nucleotide binding in protein kinase A
873 using fluorescent adenosine derivatives. *Protein Sci, 9*(9), 1818-1827.
874 doi:10.1110/ps.9.9.1818
875 Nikonova, A. S., Astsaturov, I., Serebriiskii, I. G., Dunbrack, R. L., Jr., & Golemis, E. A. (2013).
876 Aurora A kinase (AURKA) in normal and pathological cell division. *Cell Mol Life Sci,*
877 *70*(4), 661-687. doi:10.1007/s00018-012-1073-7
878 Nowakowski, J., Cronin, C. N., McRee, D. E., Knuth, M. W., Nelson, C. G., Pavletich, N. P., . . .
879 Thompson, D. A. (2002). Structures of the cancer-related Aurora-A, FAK, and EphA2
880 protein kinases from nanovolume crystallography. *Structure, 10*(12), 1659-1667.

881 Pettersen, E. F., Goddard, T. D., Huang, C. C., Couch, G. S., Greenblatt, D. M., Meng, E. C., & Ferrin,
882 T. E. (2004). UCSF Chimera--a visualization system for exploratory research and
883 analysis. *J Comput Chem, 25*(13), 1605-1612. doi:10.1002/jcc.20084
884 Sarvagalla, S., & Coumar, M. S. (2015). Structural Biology Insight for the Design of Sub-type
885 Selective Aurora Kinase Inhibitors. *Curr Cancer Drug Targets, 15*(5), 375-393.
886 Schindler, T., Bornmann, W., Pellicena, P., Miller, W. T., Clarkson, B., & Kuriyan, J. (2000).
887 Structural mechanism for STI-571 inhibition of abelson tyrosine kinase. *Science,*
888 *289*(5486), 1938-1942.
889 Seeliger, M. A., Nagar, B., Frank, F., Cao, X., Henderson, M. N., & Kuriyan, J. (2007). c-Src binds
890 to the cancer drug imatinib with an inactive Abl/c-Kit conformation and a distributed
891 thermodynamic penalty. *Structure, 15*(3), 299-311. doi:10.1016/j.str.2007.01.015
892 Steeghs, N., Eskens, F. A. L. M., Gelderblom, H., Verweij, J., Nortier, J. W. R., Ouwerkerk, J., . . .
893 de Jonge, M. J. A. (2009). Phase I Pharmacokinetic and Pharmacodynamic Study of the
894 Aurora Kinase Inhibitor Danusertib in Patients With Advanced or Metastatic Solid
895 Tumors. *Journal of Clinical Oncology, 27*(30), 5094-5101.
896 doi:10.1200/Jco.2008.21.6655
897 Taylor, S. S., Keshwani, M. M., Steichen, J. M., & Kornev, A. P. (2012). Evolution of the
898 eukaryotic protein kinases as dynamic molecular switches. *Philosophical*
899 *Transactions of the Royal Society B-Biological Sciences, 367*(1602), 2517-2528.
900 doi:10.1098/rstb.2012.0054
901 Treiber, D. K., & Shah, N. P. (2013). Ins and outs of kinase DFG motifs. *Chem Biol, 20*(6), 745-
902 746. doi:10.1016/j.chembiol.2013.06.001
903 Vajpai, N., Strauss, A., Fendrich, G., Cowan-Jacob, S. W., Manley, P. W., Grzesiek, S., & Jahnke,
904 W. (2008). Solution conformations and dynamics of ABL kinase-inhibitor complexes
905 determined by NMR substantiate the different binding modes of imatinib/nilotinib
906 and dasatinib. *J Biol Chem, 283*(26), 18292-18302. doi:10.1074/jbc.M801337200
907 Vogtherr, M., Saxena, K., Hoelder, S., Grimme, S., Betz, M., Schieborr, U., . . . Schwalbe, H.
908 (2006). NMR characterization of kinase p38 dynamics in free and ligand-bound
909 forms. *Angew Chem Int Ed Engl, 45*(6), 993-997. doi:10.1002/anie.200502770
910 Willemsen-Seegers, N., Uitdehaag, J. C., Prinsen, M. B., de Vetter, J. R., de Man, J., Sawa, M., . . .
911 Zaman, G. J. (2017). Compound Selectivity and Target Residence Time of Kinase
912 Inhibitors Studied with Surface Plasmon Resonance. *J Mol Biol, 429*(4), 574-586.
913 doi:10.1016/j.jmb.2016.12.019
914 Wilson, C., Agafonov, R. V., Hoemberger, M., Kutter, S., Zorba, A., Halpin, J., . . . Kern, D. (2015).
915 Kinase dynamics. Using ancient protein kinases to unravel a modern cancer drug's
916 mechanism. *Science, 347*(6224), 882-886. doi:10.1126/science.aaa1823
917 Winn, M. D., Ballard, C. C., Cowtan, K. D., Dodson, E. J., Emsley, P., Evans, P. R., . . . Wilson, K. S.
918 (2011). Overview of the CCP4 suite and current developments. *Acta Crystallogr D Biol*
919 *Crystallogr, 67*(Pt 4), 235-242. doi:10.1107/S0907444910045749
920 Winter, G. (2010). xia2: an expert system for macromolecular crystallography data
921 reduction. *Journal of Applied Crystallography, 43*, 186-190.
922 doi:10.1107/S0021889809045701
923 Wojcik, J., Hantschel, O., Grebien, F., Kaupe, I., Bennett, K. L., Barkinge, J., . . . Koide, S. (2010).
924 A potent and highly specific FN3 monobody inhibitor of the Abl SH2 domain. *Nat*
925 *Struct Mol Biol, 17*(4), 519-527. doi:10.1038/nsmb.1793

926 Zhao, B., Smallwood, A., Yang, J., Koretke, K., Nurse, K., Calamari, A., . . . Lai, Z. (2008).
927 Modulation of kinase-inhibitor interactions by auxiliary protein binding:
928 crystallography studies on Aurora A interactions with VX-680 and with TPX2. *Protein*
929 *Sci, 17*(10), 1791-1797. doi:10.1110/ps.036590.108
930 Zheng, H., Cooper, D. R., Porebski, P. J., Shabalin, I. G., Handing, K. B., & Minor, W. (2017).
931 CheckMyMetal: a macromolecular metal-binding validation tool. *Acta Crystallogr D*
932 *Struct Biol, 73*(Pt 3), 223-233. doi:10.1107/S2059798317001061
933 Zorba, A., Buosi, V., Kutter, S., Kern, N., Pontiggia, F., Cho, Y. J., & Kern, D. (2014). Molecular
934 mechanism of Aurora A kinase autophosphorylation and its allosteric activation by
935 TPX2. *Elife, 3*, e02667. doi:10.7554/eLife.02667

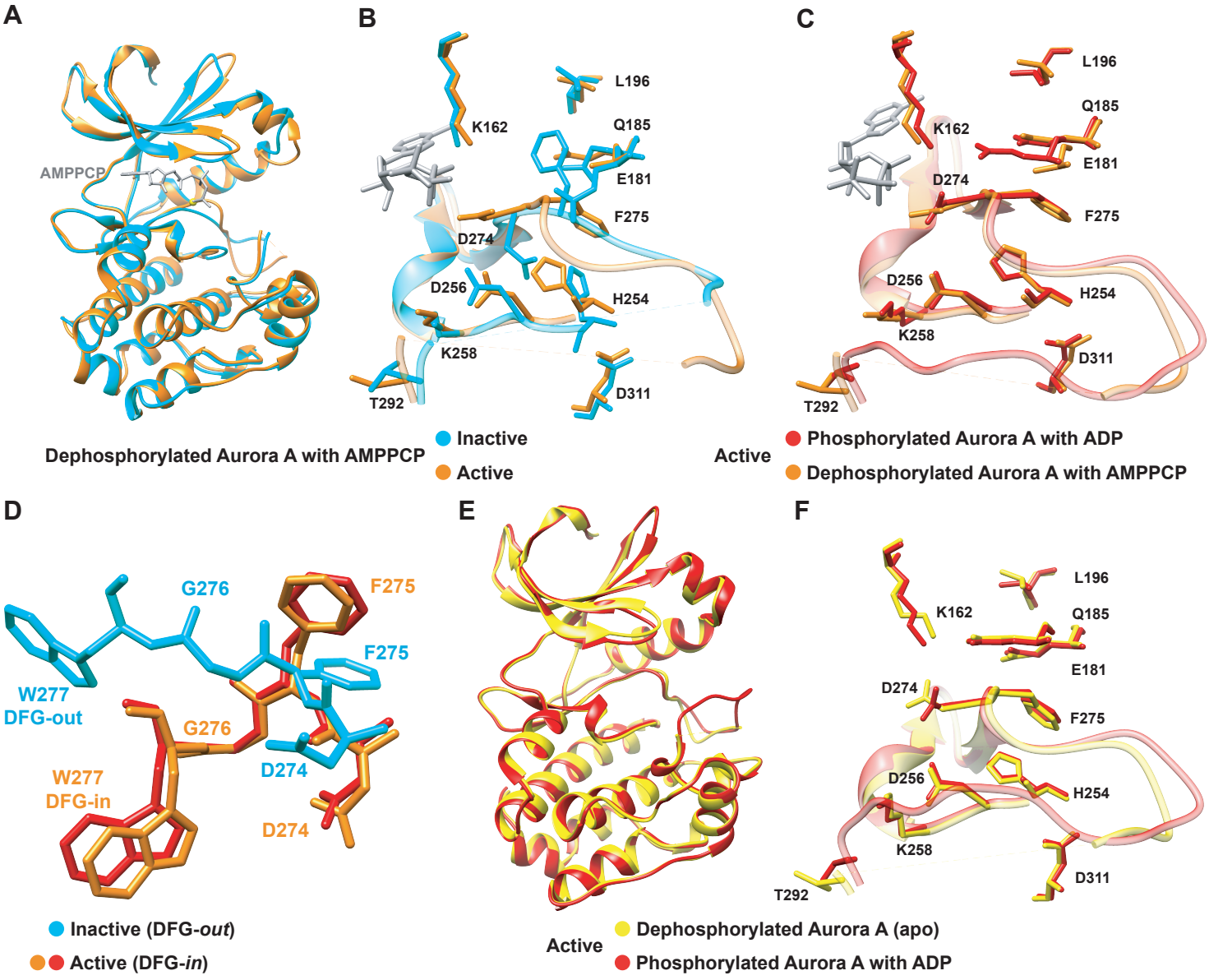

Figure 1. Dephosphorylated Aurora A samples both the active and inactive conformation. (A) Superposition of X-ray structures of dephosphorylated Aurora A (residues 122-403) with Mg^{2+}.AMPPCP (AMPPCP in gray sticks and magnesium as yellow sphere) in the inactive (cyan, PDB 4C3R (Zorba et al., 2014)) and active (orange, PDB 6CPF) state, solved from crystals of the same crystallization well. (B) Zoom-in of (A) to visualize the nucleotide binding region (K162, D274, and E181), the R-spine (L196, Q185, F275, H254, and D311) and the activation loop region (D256, K258, and T292). (C) Same zoom-in as in (B), but dephosphorylated Aurora A in active state (orange) is superimposed with phosphorylated Aurora A (red, PDB 1OL7 (Bayliss et al., 2003)). (D) Superposition of the DFG(W) motif in the three states shown in (B) and (C).(E) Superposition of phosphorylated Aurora A in active conformation (red) and apo, dephosphorylated Aurora A also in the active conformation (yellow, PDB 6CPE). (F) Zoom-in of (E) showing the same region as in (B).

Data collection and refinement statistics for dephosphorylated Aurora A

	apo-Aurora A (6CPE)	Aurora A + AMPPCP (6CPF)
Data collection		
Space group	P 61 2 2	P 61 2 2
Cell dimensions		
a, *b*, *c* (Å)	80.55, 80.55, 169.79	81.75, 81.75, 172.87
α, β, γ (°)	90, 90, 120	90, 90, 120
Resolution (Å)	84.90 – 2.45 (2.55 – 2.45)[a]	86.44 – 2.30 (2.39 – 2.30)[a]
R_{meas}	0.073 (1.308)	0.113 (2.260)
$I/\sigma(I)$	15.0 (1.6)	10.3 (1.3)
$CC_{1/2}$	0.998 (0.711)	0.997 (0.465)
Completeness (%)	99.9 (100)	100 (100)
Redundancy	7.6 (6.3)	9.7 (7.8)
Refinement		
Resolution (Å)	64.52 – 2.45	54.79 – 2.30
No. reflections	12617 (1224)	15756 (1527)
R_{work} / R_{free}	0.2151 / 0.2528	0.2179 / 0.2587
No. atoms		
Protein	2035	2055
Ligand/ion	11	32
Water	4	6
B factors		
Protein	71.83	63.68
Ligand/ion	75.77	76.44
Water	52.52	45.84
R.m.s. deviations		
Bond lengths (Å)	0.005	0.004
Bond angles (°)	0.98	0.97

The number of crystals for each structure is 1.
[a] Values in parentheses are for highest-resolution shell.

Figure 1-*figure supplement 1*

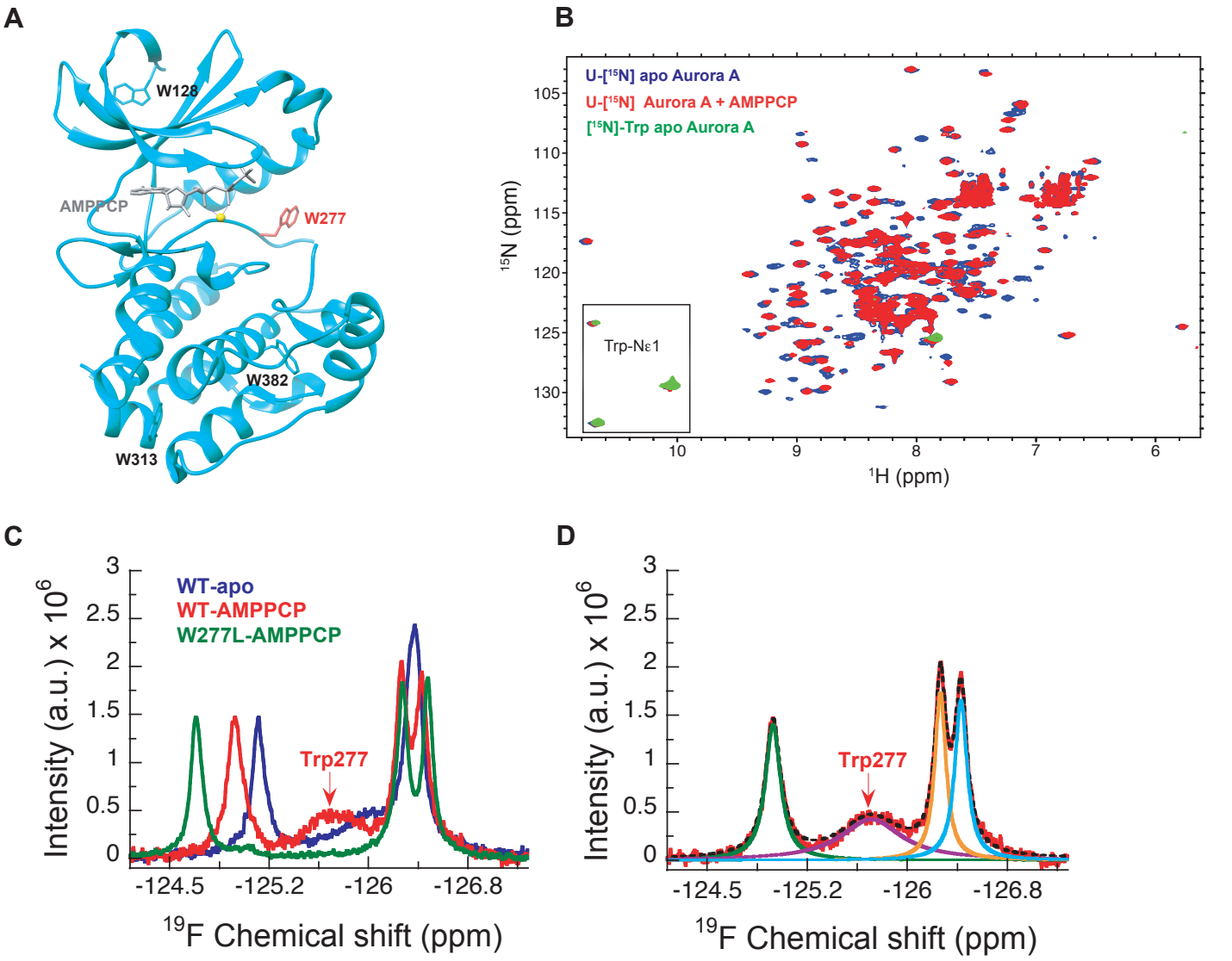

Figure 2. NMR spectra indicate extensive dynamics of the DFG-loop. (A) The four tryptophan residues in Aurora A are shown on the structure (PDB 4C3R (Zorba et al., 2014)) in stick representation; Trp277 in the DFGW-loop is highlighted in red. (B) Overlay of [^{1}H-^{15}N]-TROSY-HSQC spectra of dephosphorylated Aurora A in its apo-state (U-[^{15}N], blue; [^{15}N]-Trp, green) and AMPPCP-bound (U-[^{15}N], red). Only three instead of the four expected cross peaks for tryptophan side chains are detected. (C) ^{19}F NMR spectra of 5-fluoro-Trp labeled dephosphorylated wild-type Aurora A (apo in blue and AMPPCP-bound in red) and the W277L Aurora A mutant bound to AMPPCP (green). The assignment of Trp277 following the DFG-loop is shown. (D) ^{19}F spectrum of wild-type Aurora A bound to AMPPCP (red) together with its deconvolution into four Lorentzian line shapes, the overall fit is shown as a black, dotted line. The integrals for all four signals are equal, but the linewidth for Trp277 (purple) is approximately 5-fold larger.

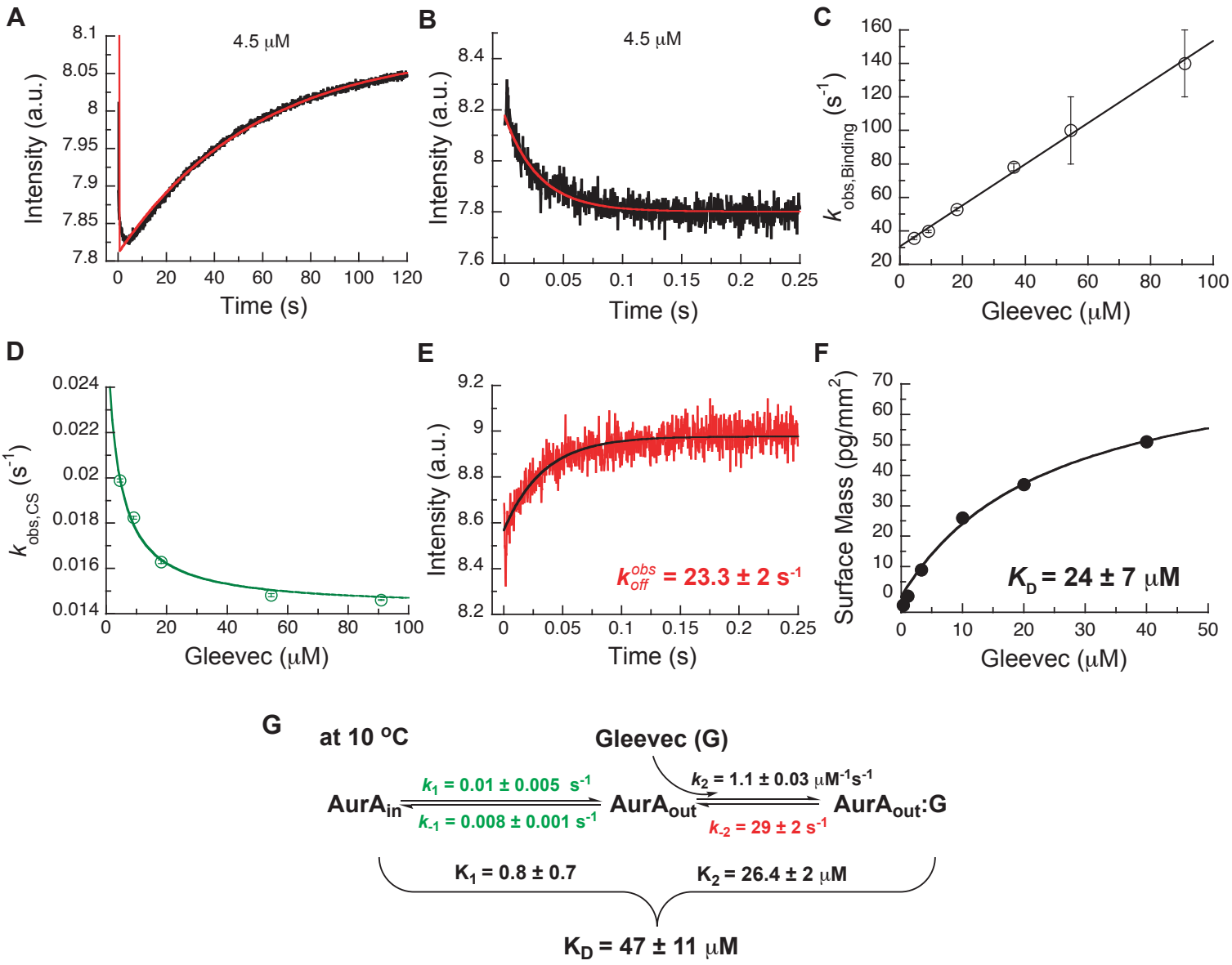

Figure 3. Kinetics of Gleevec binding to Aurora A at 10 °C measured by stopped-flow Trp fluorescence to dissect all binding steps. (A) Kinetics after mixing 0.5 μM Aurora A with 4.5 μM Gleevec is double exponential with a fast decrease and a slow increase in fluorescence signal. (B) The decrease in fluorescence intensity due to the fast binding phase was completed within 0.25 s. (C) Observed rate constants of fast binding phase were plotted against increasing concentrations of Gleevec ($k_{obs,Binding}$ = 1.1 ± 0.3 $\mu M^{-1}s^{-1}$, k_{diss} = 31 ± 2 s^{-1} from the y-intercept). (D) The increase in fluorescence intensity of slow phase (A) is attributed to conformational selection. The plot of $k_{obs,CS}$ of this slow phase versus Gleevec concentration was fit to Equation 1 and yields k_1= 0.014 ± 0.001 s^{-1} and k_{-1} = 0.011 ± 0.002 s^{-1}. (E) Dissociation kinetics of pre-incubated solution with 5 μM Aurora A and 5 μM Gleevec measured by stopped-flow fluorescence after an 11-fold dilution of the complex yields the k_{-2} = 23.3 ± 2 s^{-1}. (F) The macroscopic dissociation constant (K_D) of Gleevec binding to Aurora A measured by Creoptix WAVE. (G) Gleevec (labeled as G) binding scheme to Aurora A corresponds to a two-step binding mechanism: conformational selection followed by the physical binding step. The corresponding microscopic rate constants obtained from the global fit and calculated overall equilibrium and dissociation constants are shown. Fluorescence traces are the average of at least five replicate measurements (n > 5), and error bars and uncertainties given in C-G denote the (propagated) standard deviation in the fitted parameter.

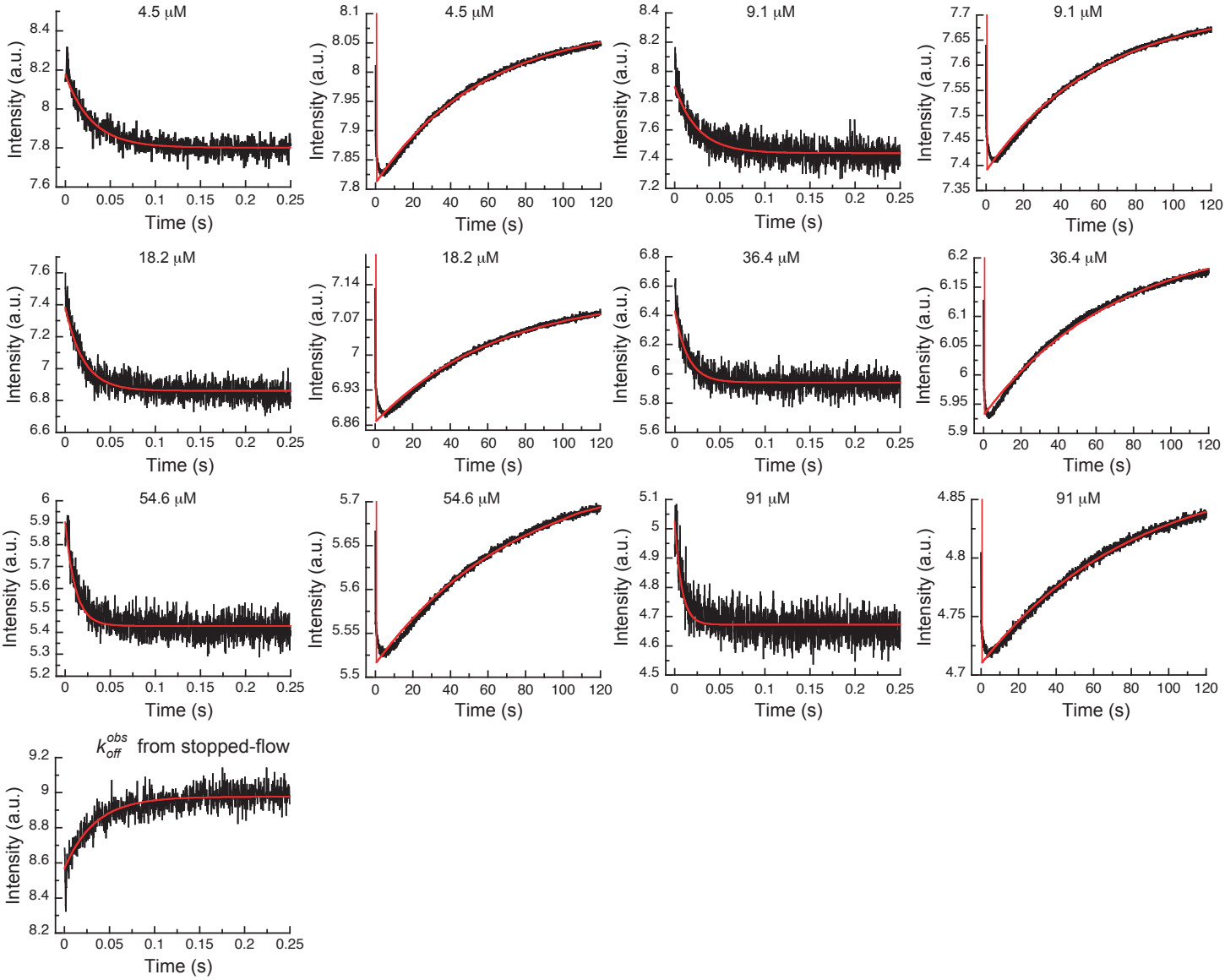

Figure 4. Global fits of Gleevec binding- and dissociation-kinetics to Aurora A at 10 °C. Fitting of kinetic traces (average, n > 5) of the mixing of 0.5 μM Aurora A with different Gleevec concentrations at two timescales, 0.25 s and 120 s, and dissociation kinetics (k_{off}) were performed using the KinTek Explorer software with the binding scheme in Figure 3G. Red lines show the results of the global fit to the experimental data in black.

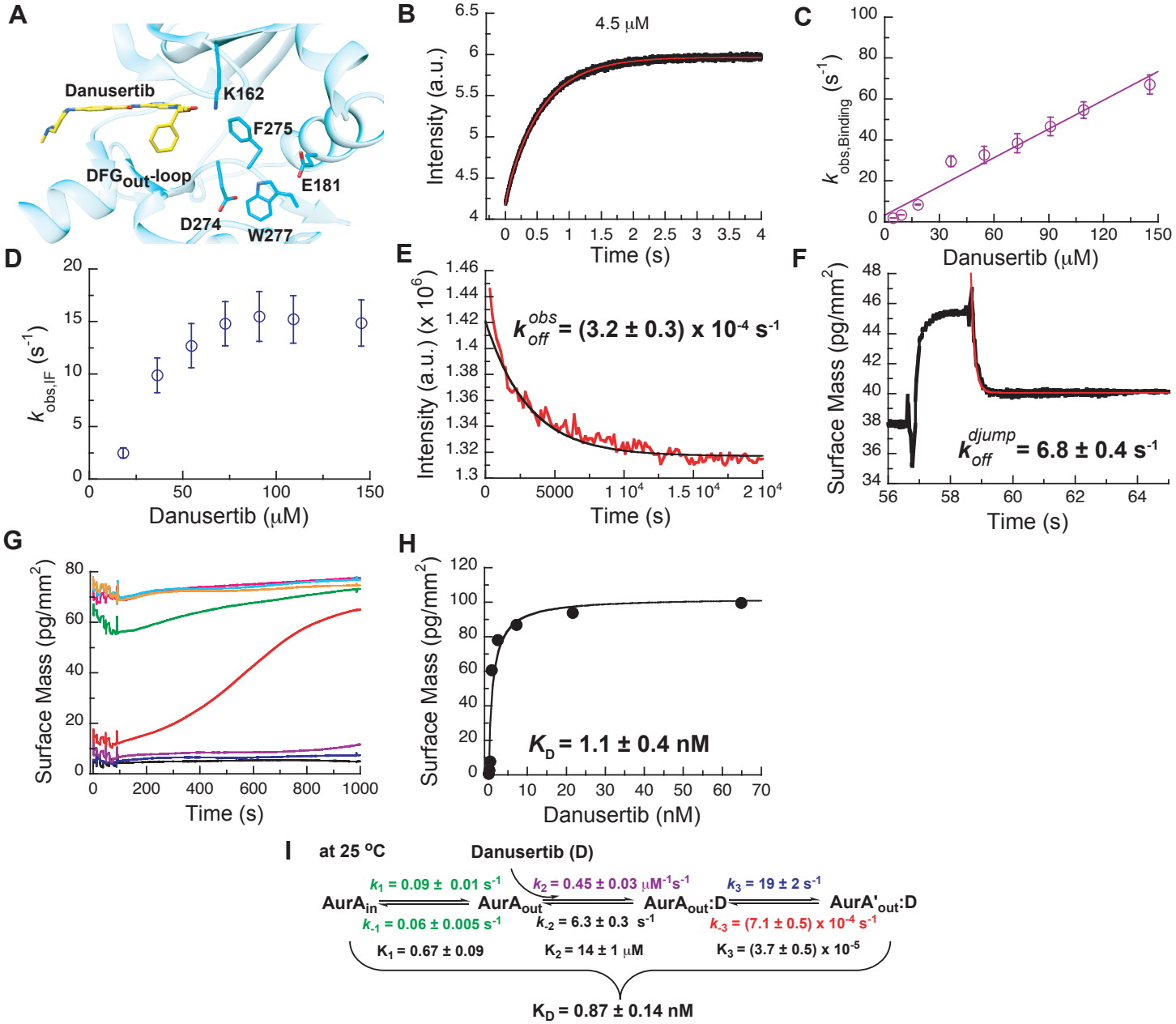

Figure 5. Mechanism of Danusertib binding to Aurora A at 25 °C. (A) Danusertib bound to the DFG-*out* conformation of Aurora A is shown highlighting important active-site residues in stick representation (PDB 2J50 (Fancelli et al., 2006)). (B) The increase in fluorescence upon Danusertib binding is fitted to a double exponential. (C) Plot of $k_{obs,Binding}$ versus the concentration of Danusertib for the fast phase yields k_2 = 0.4 ± 0.1 $\mu M^{-1}s^{-1}$ and k_{-2} = 4.6 ± 3 s^{-1} and the $k_{obs,IF}$ for the slow phase (D) reaches a plateau around 16 ± 2 s^{-1}. (E) Dissociation of Danusertib from Aurora A at 25 °C after a 30-fold dilution of the Aurora A/Danusertib complex measured by Trp-fluorescence quenching and fitting with single exponential gives a value of k_{-3} = (3.2 ± 0.3) x 10^{-4} s^{-1}.(F) Double-jump experiment (2 s incubation time of 1 μM Danusertib to Aurora A followed by 60 s long dissociation step initiated by a wash with buffer) was measured by Creoptix WAVE waveguide interferometry to properly define the value of k_{-2} = 6.8 ± 0.4 s^{-1}. (G) Macroscopic dissociation constant (K_D) determined by Creoptix WAVE waveguide interferometry: surface-immobilized Aurora A was incubated with various concentrations of Danusertib (0.1 nM (black), 0.2 nM (blue), 0.4 nM (purple), 0.8 nM (red), 2.4 nM (green), 7.2 nM (pink), 21.6 nM (cyan), and 64.8 nM (orange)) and surface mass accumulation was observed until establishment of equilibrium. (H) A plot of the final equilibrium value versus Danusertib concentration yields a K_D = 1.1 ± 0.4 nM. (I) Binding scheme of Danusertib (labeled D) highlighting a three-step binding mechanism, containing both conformational selection and induced-fit step. Red lines in (B, F) and black line in (E) are the results from global fitting. Kinetic constants shown in I determined from global fitting (Figure 6). Fluorescence traces are the average of at least five replicate measurements (n > 5), and error bars and uncertainties given in C-E, H,and I denote the (propagated) standard deviation in the fitted parameter.

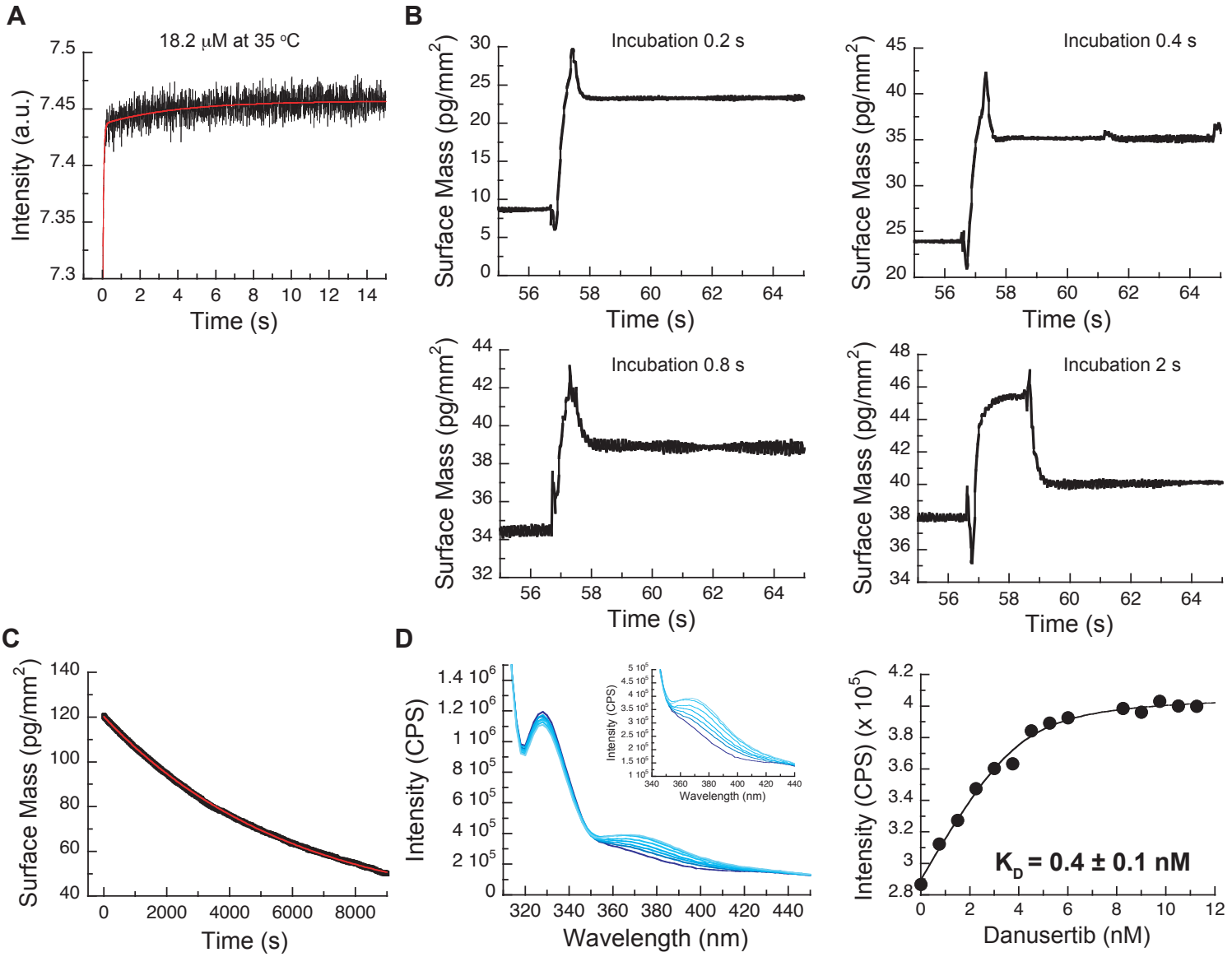

Figure 5-*figure supplement 1*. (A) Kinetic trace at 35 °C of 18.2 μM Danusertib binding to 0.1 μM Aurora A. The red line represents the best fit of the trace to a double exponential function. The initial fast increase in fluorescence is a convolution of the fast binding and induced-fit steps, whereas the slower phase gives an observed rate constant of approximately 0.1 s^{-1}, suggestive of a third process (i.e., conformational selection). (B) Double-jump experiments measured with Creoptix WAVE waveguide intereferometry at 25 °C using Danusertib and a 0.2, 0.4, 0.8 and 2 s incubation time. In the first step of the double jump, Danusertib is incubated with surface-immobilized Aurora A kinase before washing with buffer alone initiates dissociation in a second step. All traces show a single exponential decay with an observed rate constant of 6 s^{-1} and its amplitude increases with longer incubation time as more $AurA_{out}$:D is formed. (C) Dilution of the Aurora A/Danusertib complex formed after 1 hour incubation. The slow dissociation of Aurora A/Danusertib (limited by k_{-3}) was measured by Creoptix WAVE waveguide interferometry and fitted to a single exponential with a value of k_{-3} = (2 ± 0.6) x 10^{-4} s^{-1}. (D) Representative selection of emission spectra obtained after the addition of increasing concentrations of Danusertib (0 - 11.25 nM from dark to light blue) to Aurora A (excitation at 295 nm). Plot of the increase in fluorescence intensity at 368 nm versus Danusertib concentration yields a K_D value of 0.4 ± 0.1 nM determined by fitting the data to Equation 6. Fluorescence trace in A is the average of five replicate measurements (n = 5), and the uncertainties given in D denotes the standard deviation in the fitted parameter.

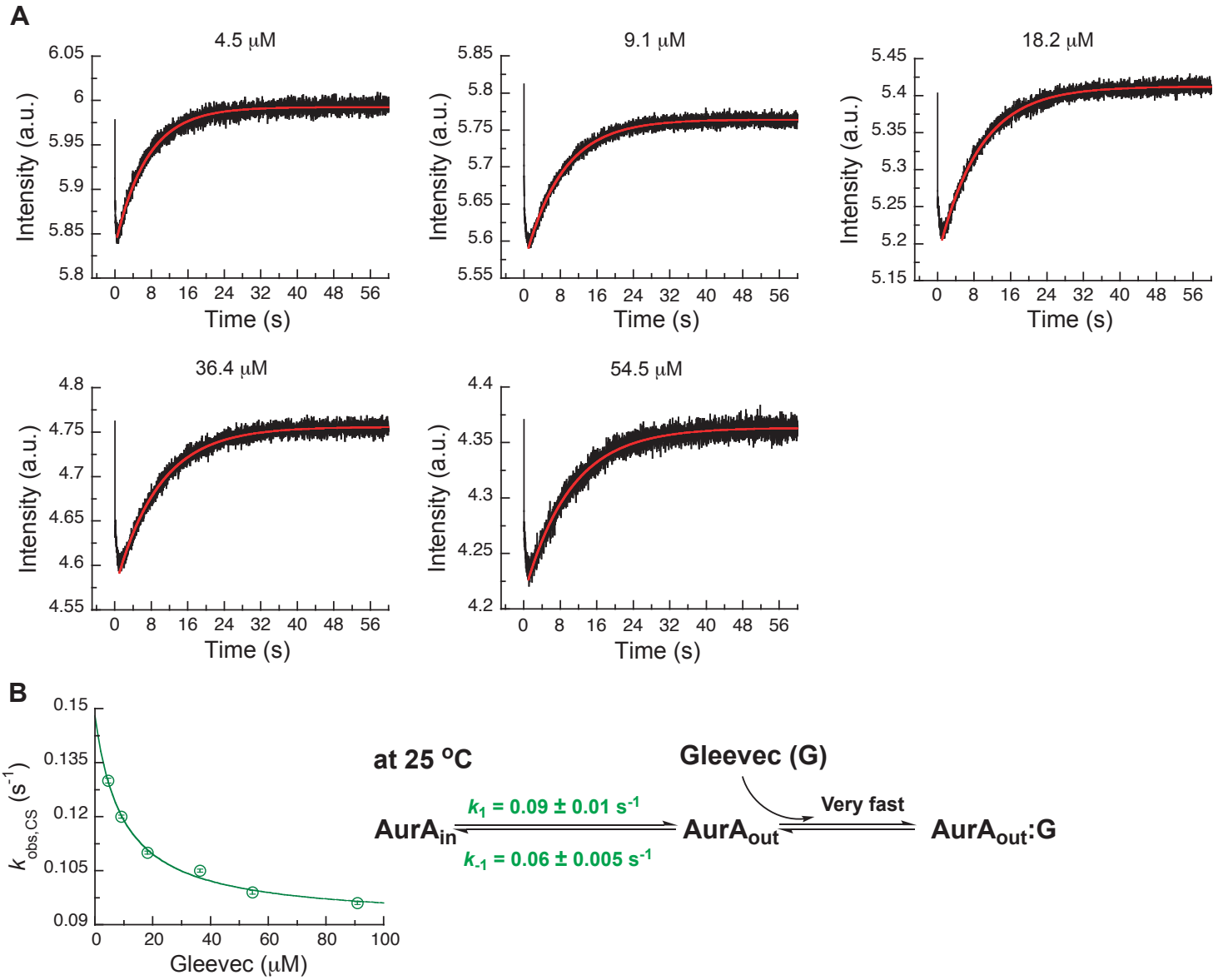

Figure 5-*figure supplement 2*. Kinetics of Gleevec binding to Aurora A at 25 °C to determine DFG-*in*/DFG-*out* equilibrium in apo Aurora A at 25 °C. (A) 0.5 μM Aurora A was mixed with shown Gleevec concentrations. The increase in fluorescence intensity of slow phase reflects the conformational selection step (see Figure 3A). (B) $k_{obs,CS}$ of the slow phase as a function of the Gleevec concentration is an inverse hyperbolic function and fitting to Equation 1 gives k_1 = 0.09 ± 0.01 s^{-1} and k_{-1} = 0.06 ± 0.005 s^{-1}. Corresponding binding scheme is depicted. Fluorescence traces are the average of at least five replicate measurements (n > 5), and error bars and uncertainties given in B denote the standard deviation in the fitted parameter.

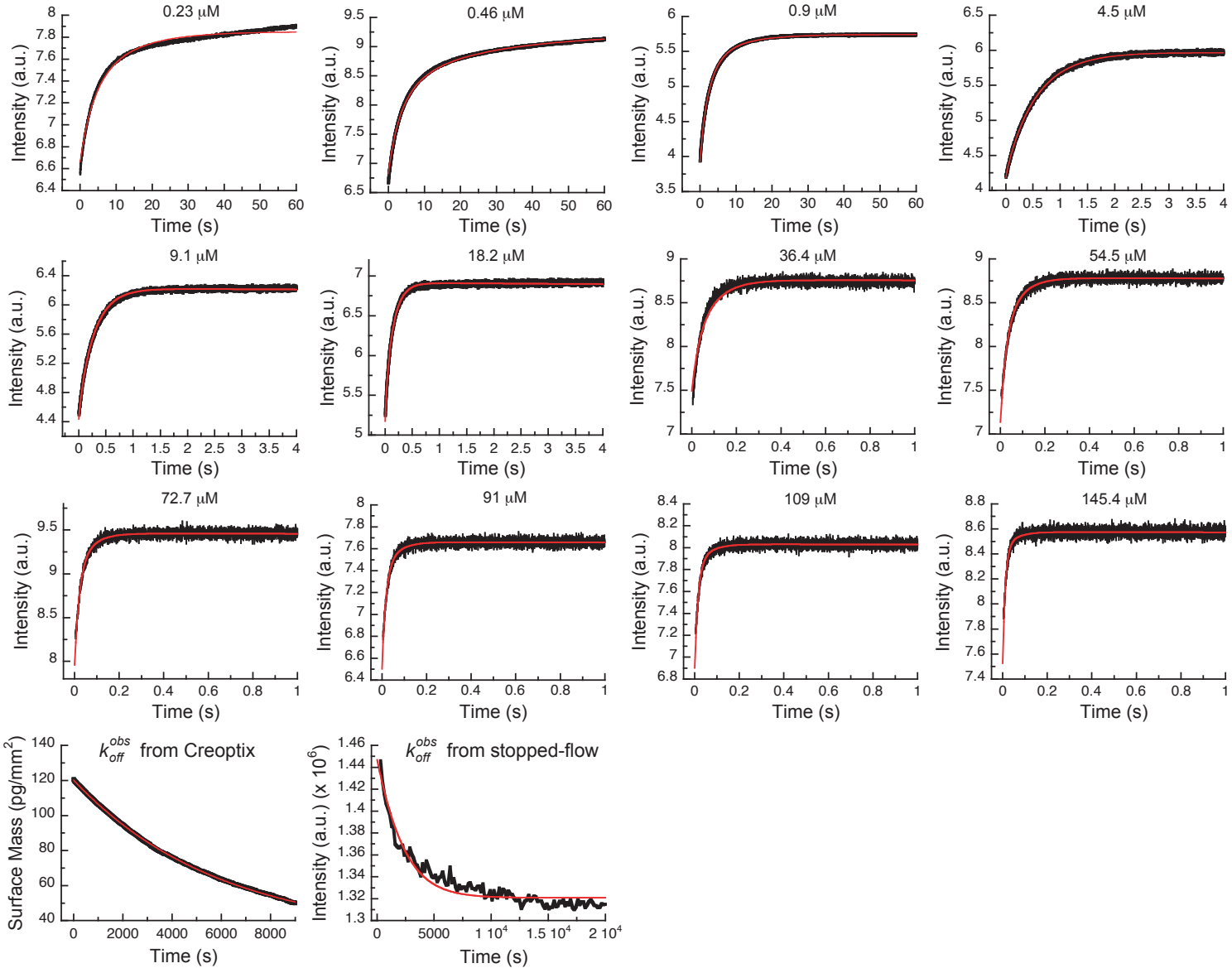

Figure 6. Global fits of Danusertib binding and dissociation kinetics to Aurora A at 25 °C. Binding kinetics was monitored by stopped-flow fluorescence for different concentrations of Danusertib (indicated) to 0.5 μM Aurora A, and dissociation kinetics ($k_{obs,off}$) by Creoptix and fluorimeter (see Figure 5). Fluorescence traces are the average of at least five replicate measurements (n > 5). Global fitting was performed using the KinTek Explorer software using the model shown in Figure 5I.

Creoptix $k^{obs}_{slow\text{-}off}$ = (2 ± 0.006) x 10^{-4} s^{-1}

Fluorimeter $k^{obs}_{slow\text{-}off}$ = (3.2 ± 0.3) x 10^{-4} s^{-1}

at 25 °C

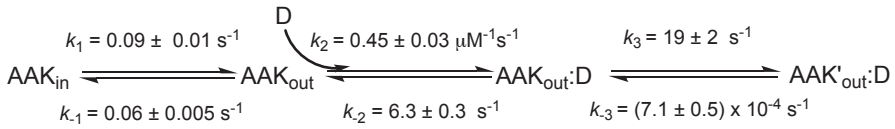

Kinetic Partitioning: Aurora A with Danusertib

$$k^{obs}_{slow\text{-}off} = \frac{k_{-2} \times k_{-3}}{k_{-2} + k_3 + k_{-3}}$$

$$= \frac{6.3 \times (7.1 \times 10^{-4})}{6.3 + 19 + (7.1 \times 10^{-4})}$$

$$k^{obs}_{slow\text{-}off} = (1.77 \pm 0.2) \times 10^{-4}\ s^{-1}$$

Figure 6-*figure supplement 1*. Kinetic partitioning of Aurora A with Danusertib. The apparent discrepancy between the experimentally observed off rates and the microscopic rate constant, k_{-3}, can be explained by considering the kinetic partitioning. Uncertainties given denote the (propagated) standard deviation in the fitted parameter.

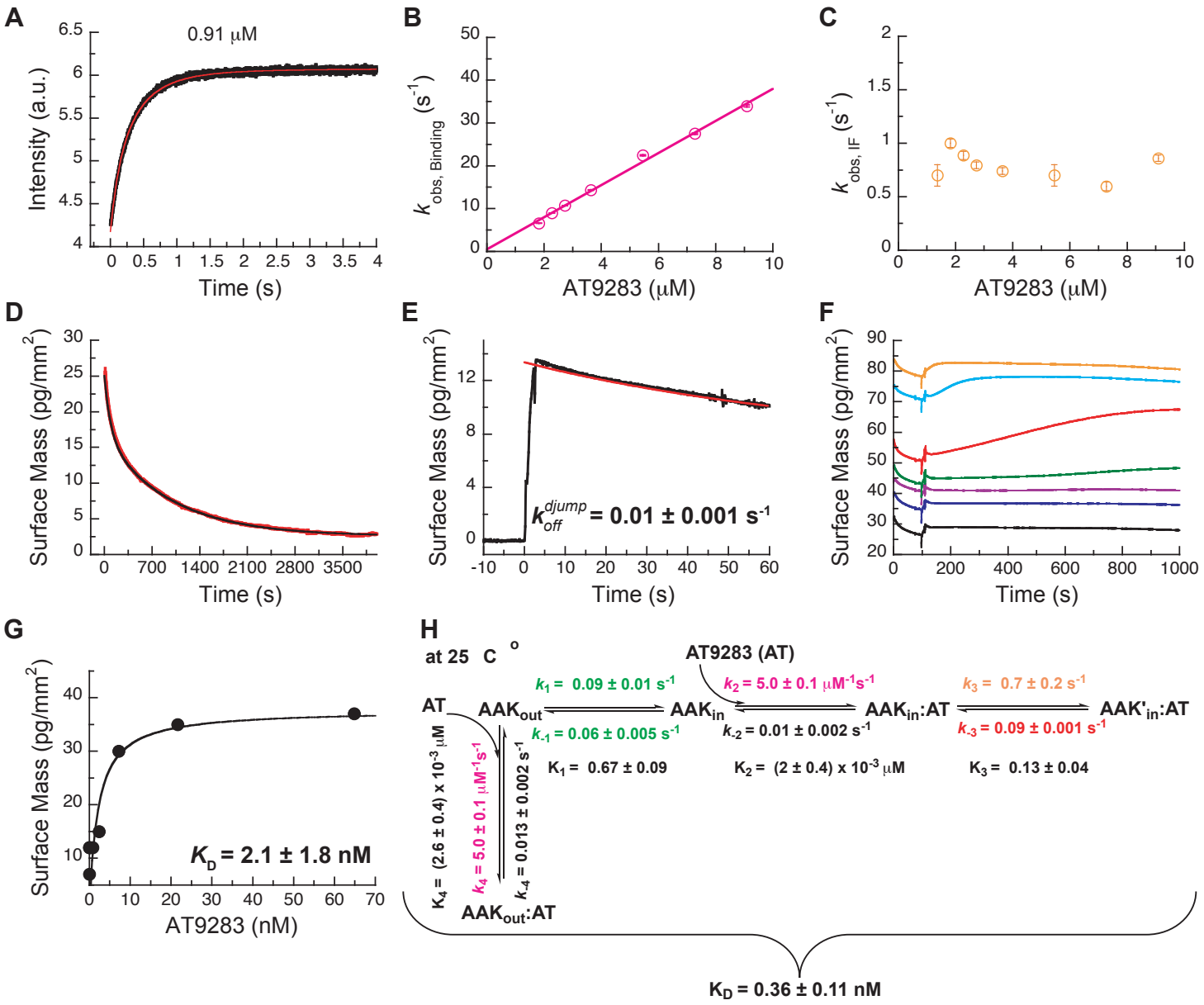

Figure 7. Mechanism of AT9283 drug binding to Aurora A at 25 °C. (A) The increase in fluorescence at 25 °C upon AT9283 binding fitted to a double exponential. (B) The plot of $k_{obs,Binding}$ versus AT9283 concentration for the fast phase yields k_2 = 3.4 ± 0.5 μM^{-1}s^{-1} and an underdetermined intercept (k_{-2}) and (C) the k_{obs} of the slow phase reaches a plateau around 0.8 ± 0.2 s^{-1}. (D) Dilution of the Aurora A/AT9283 complex formed after 1 hour incubation. The slow dissociation was measured by Creoptix WAVE waveguide interferometry and fitted with a double exponential with rate constants of (1.1 ± 0.02) x 10^{-2} s^{-1} and (0.1 ± 0.01) x 10^{-2} s^{-1}. (E) Double-jump experiments (1 s incubation time of 1 μM AT9283 to Aurora A followed by 60 s long dissociation step initiated by a wash with buffer) was measured by Creoptix WAVE waveguide interferometry to properly define the value of k_{-2} = (1.0 ± 0.1) x 10^{-2} s^{-1}. (F) Macroscopic dissociation constant (K_D) determined by Creoptix WAVE waveguide interferometry: surface-immobilized Aurora A was incubated with various concentration of AT9283 (0.03 nM (black), 0.27 nM (blue), 0.8 nM (purple), 2.4 nM (green), 7.2 nM (red), 21.6 nM (cyan), and 64.8 nM (orange)) and surface mass accumulation was observed until establishment of equilibrium. (G) A plot of the final equilibrium value versus AT9283 concentration yields a K_D = 2.1 ± 1.8 nM. (H) Binding scheme for AT9283 (labeled AT) highlighting a four-steps binding mechanism, that contains binding to two different states, a conformational selection mechanism and an induced-fit step. Kinetic constants shown in H were determined from global fitting (see Figure 8). Fluorescence traces are the average of at least five replicate measurements (n > 5), and error bars and uncertainties given in B,C,G and H denote the (propagated) standard deviation in the fitted parameter.

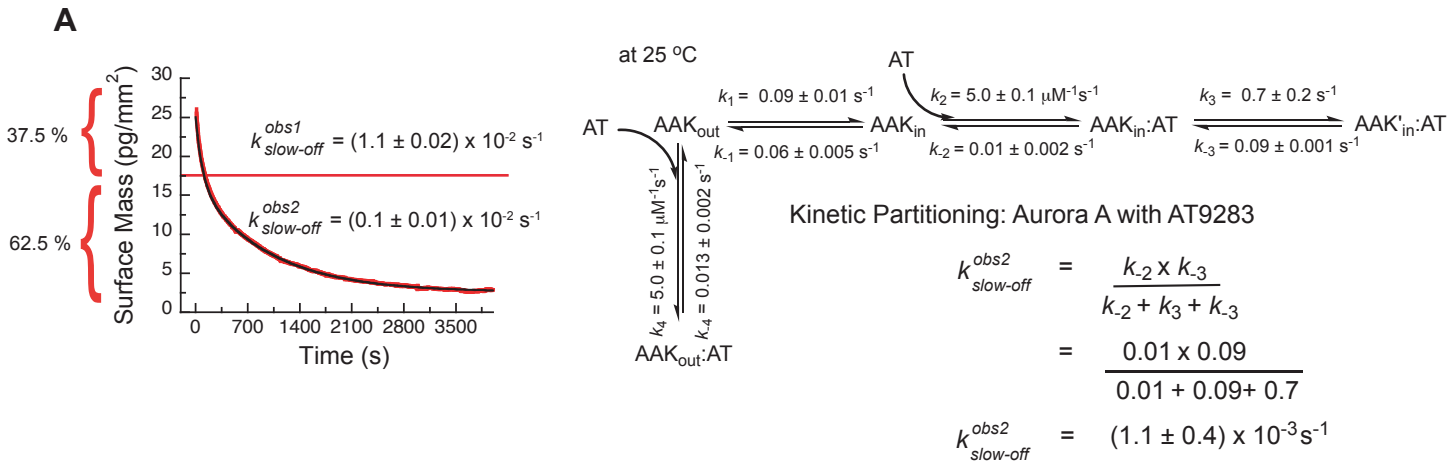

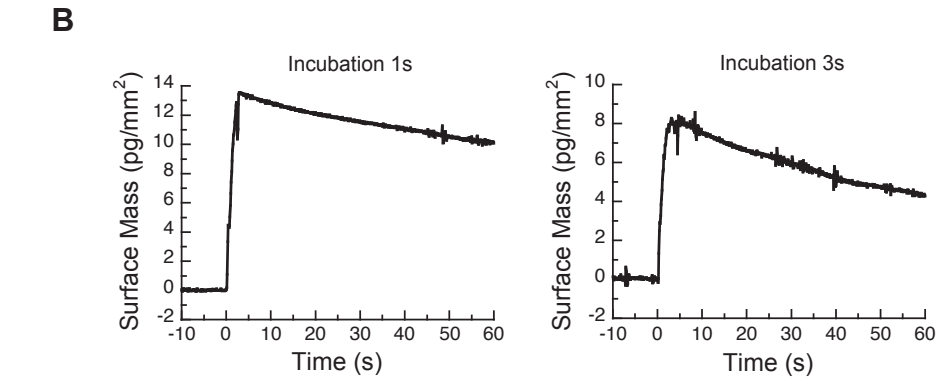

Figure 7-*figure supplement 1*. (A) Kinetic partitioning of Aurora A with AT9283. The apparent discrepancy between the experimentally observed off rates and the microscopic rate constant, k_{-3}, can be explained by considering the kinetic partitioning. (B) Double-jump experiments measured by Creoptix WAVE waveguide interferometry at 25 °C of AT9283 at 1 and 3 s incubation time before induction of dissociation by a buffer wash are best described with a single exponential function of (k = 0.01 s^{-1}). Uncertainties given in A denote the (propagated) standard deviation in the fitted parameter.

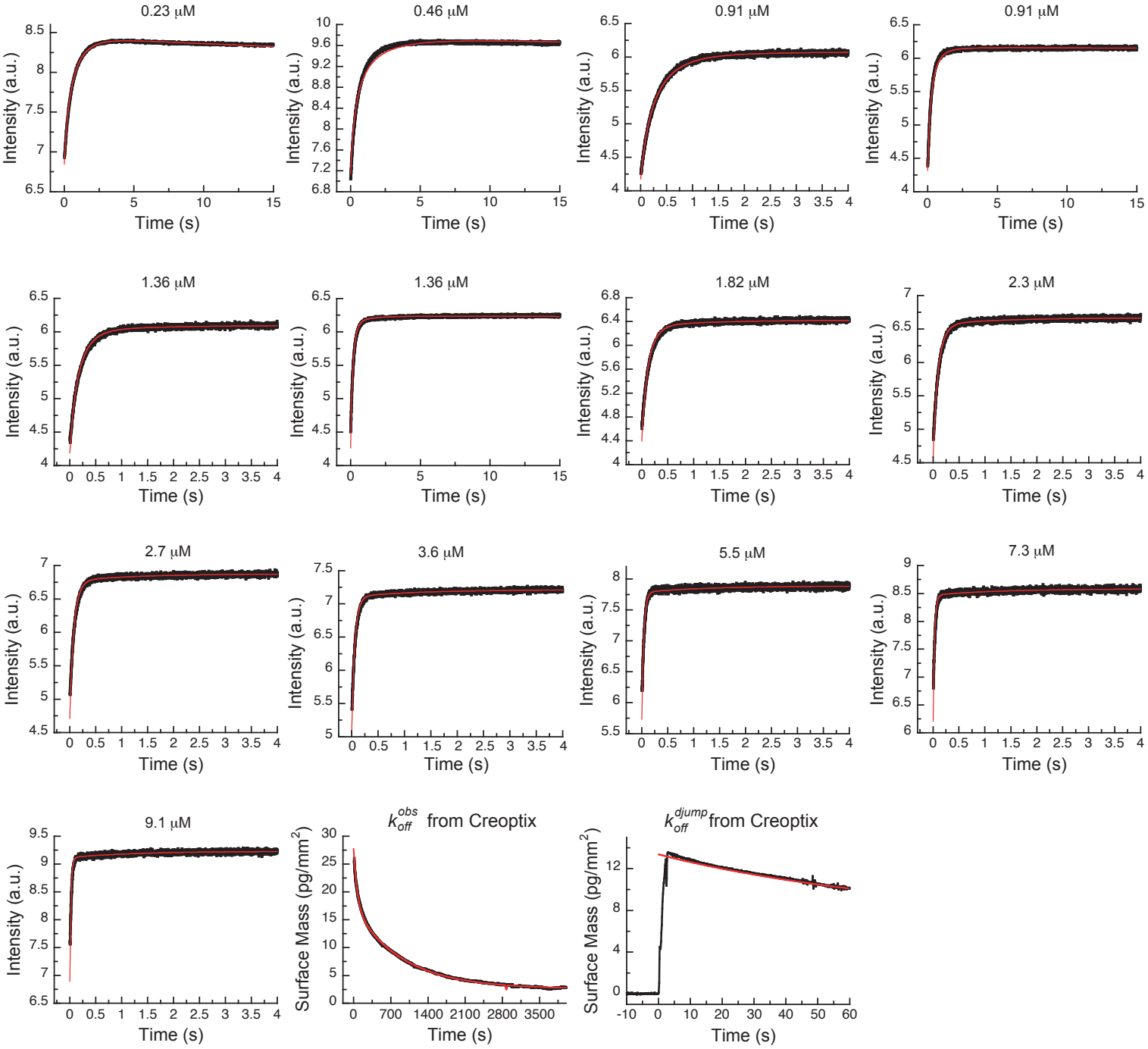

Figure 8. Global fits of AT9283 binding and dissociation kinetics to Aurora A at 25 °C. Binding kinetics was monitored by stopped-flow fluorescence at different concentrations of AT9283 (indicated) to 0.5 μM Aurora A. Dissociation kinetics were obtained for fully equilibrated drug/kinase complex ($k_{obs,off}$) or for the initial encounter complex ($k_{off,djump}$) by using a 1 hour or a short 2 s incubation of the kinase with AT9283, respectively, before inducing dissociation by a buffer wash using Creoptix WAVE waveguide interferometry. Global fitting was performed with KinTek Explorer software using the model in Figure 7H (reduced χ^2 = 3.2). Fluorescence traces are the average of at least five replicate measurements (n > 5).

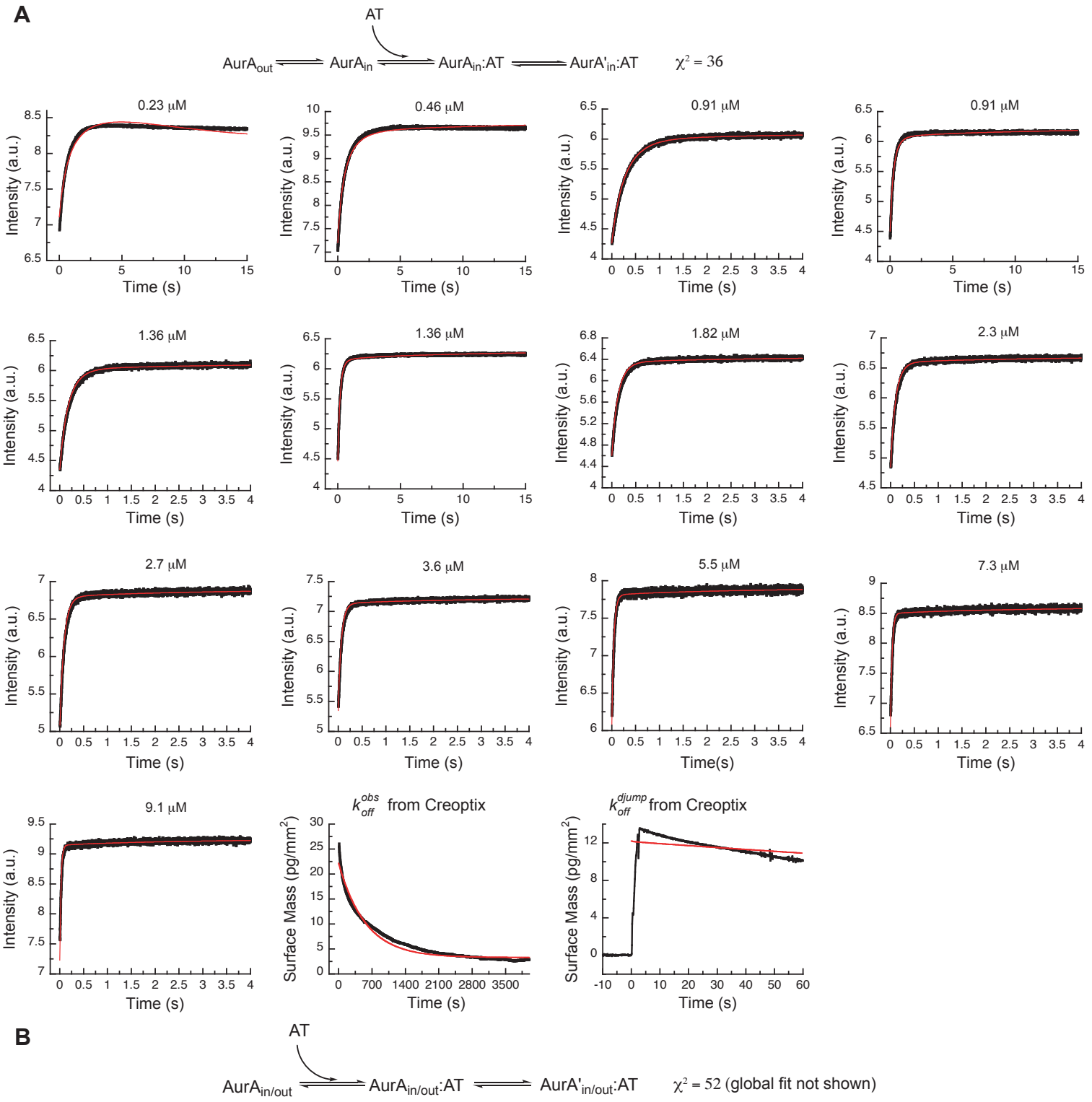

Figure 8-*figure supplement 1*. Alternative binding models of AT9283 to Aurora A cannot explain the experimental data. (A) Our initial three-state binding scheme, where AT9283 binds only the DFG_{in} state of Aurora A and is followed by an induced-fit step, is incorrect. The best global fit (shown in red) did not describe the data as can be seen by visual inspection and from the reduced χ^2 value of 36. (B) An alternative model, where AT9283 can bind to Aurora A irrespective of the state of the DFG-loop, and binding is followed by an induced-fit step did not result in adequate fits (data not shown) and a reduced χ^2 value of 52. In both cases the values for the interconversion between $AurA_{out}$ and $AurA_{in}$ were taken from the Gleevec experiment (Figure 5-*figure supplement 2*). Fluorescence traces are the average of at least five replicate measurements (n > 5).

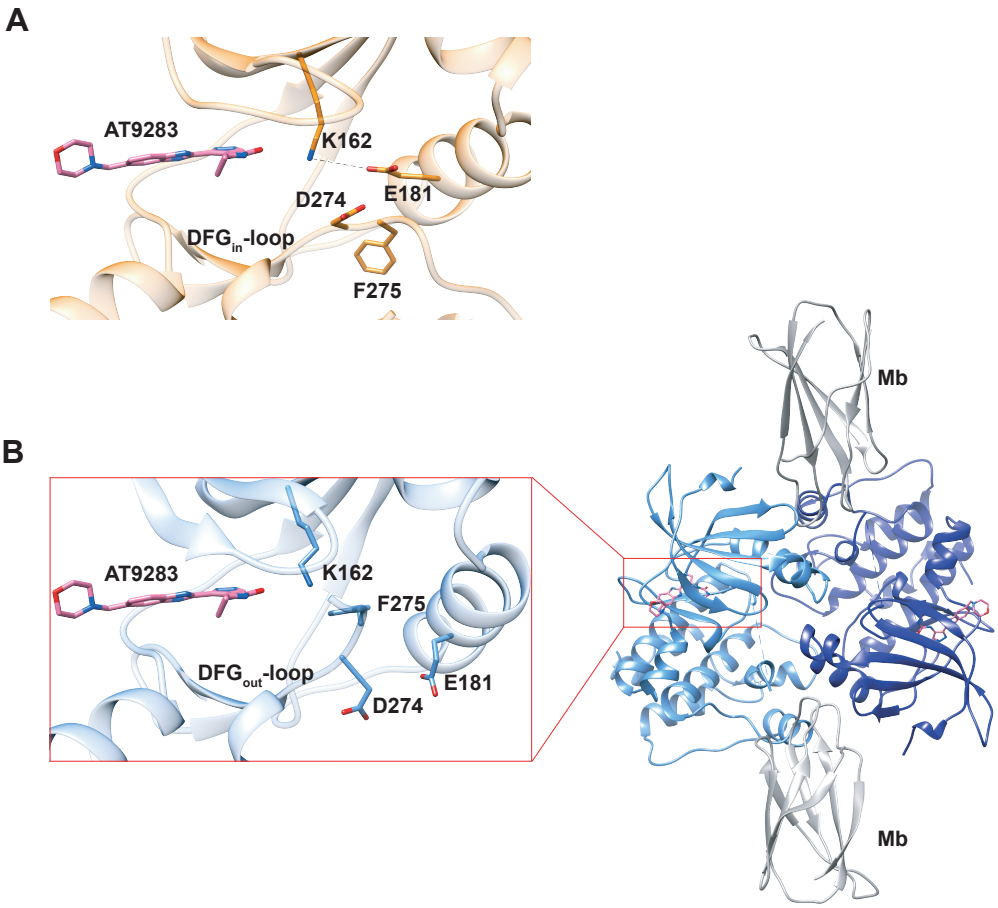

Figure 9. X-ray structures of Aurora A bound to inhibitor AT9283 reveal multiple binding modes. (A) AT9283 (pink) bound to the active site of Aurora A (PDB 2W1G, (Howard et al., 2009)) shows the DFG_{in}-loop conformation and a salt bridge between K162 and E181. (B) Aurora A dimer (light and dark blue ribbon) in complex with AT9283 (pink) and inhibiting monobody (Mb, grey), showing DFG_{out}-loop and broken K162 and E181 salt bridge (PDB 6CPG).

Data collection and refinement statistics for dephosphorylated Aurora A in complex with monobody and AT9283

	Aurora A + Mb + AT9283 (6CPG)
Data collection	
Space group	P 21 21 21
Cell dimensions	
a, *b*, *c* (Å)	63.86, 69.7, 175.56
α, β, γ (°)	90, 90, 90
Resolution (Å)	43.14 – 2.80 (2.87 – 2.80)[a]
R_{meas}	0.189 (1.268)
$I/\sigma(I)$	8.9 (1.1)
$CC_{1/2}$	0.986 (0.625)
Completeness (%)	99.2 (98.8)
Redundancy	5.4 (5.3)
Refinement	
Resolution (Å)	36.17 – 2.80
No. reflections	19556 (1845)
R_{work} / R_{free}	0.2792/ 0.3350
No. atoms	
Protein	5122
Ligand/ion	56
Water	
B factors	
Protein	78.84
Ligand/ion	81.05
Water	
R.m.s. deviations	
Bond lengths (Å)	0.003
Bond angles (°)	0.98

The number of crystals for each structure is 2.
[a] Values in parentheses are for highest-resolution shell.

Figure 9-*figure supplement 1*

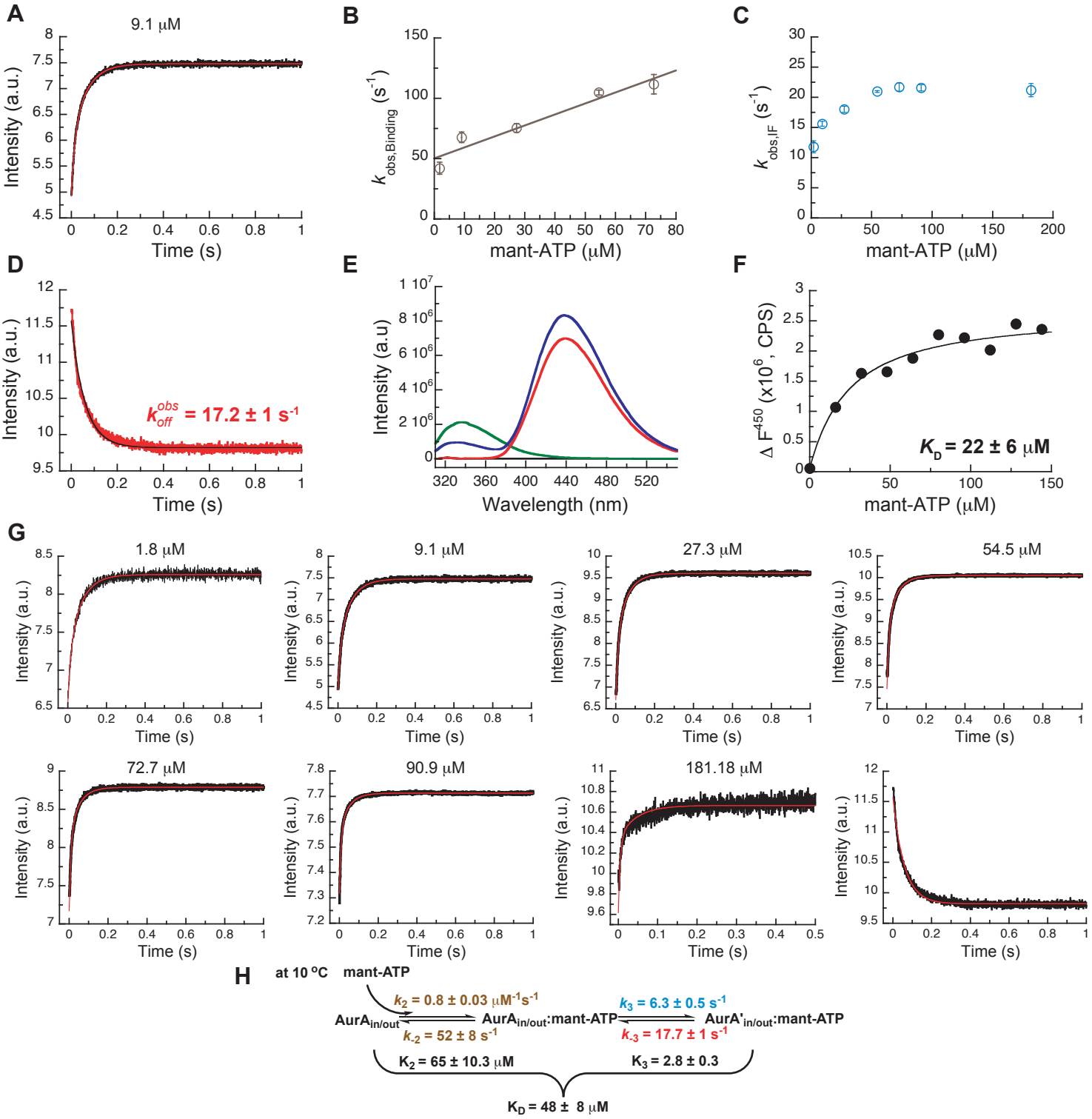

Figure 10. Mechanism of ATP binding to Aurora A at 10 °C. (A) Binding of mant-ATP to Aurora A was followed by an increase in fluorescence with biphasic kinetics. The plot of k_{obs} versus concentration of mant-ATP of fast phase (B) yields k_2 = 0.8 ± 0.2 $μM^{-1}s^{-1}$ and k_{-2} = 50 ± 8 s^{-1} and the slow phase (C) reached a plateau around 21 ± 1 s^{-1} (k_3 + k_{-3}). (D) Dissociation kinetics of 10 μM Aurora A/10 μM mant-ATP complex was measure after a 10-fold dilution into buffer and yields $k_{obs,off}$ = 17.2 ± 1 s^{-1}. (E, F) Macroscopic dissociation constant of Aurora A with mant-ATP measured by fluorescence energy transfer. (E) Emission spectra (excitation at 290 nm) of 1 μM Aurora A (green), 160 μM mant-ATP (red), and 1 μM Aurora A/160 μM mant-ATP (blue). (F) The change in fluorescence at 450 nm (ΔF450) versus mant-ATP concentrations yields K_D = 22 ± 6 μM. (G) Global fitting (red) of all kinetics data (black) in KinTek Explorer to the binding scheme shown in (H) results in the kinetic constants given in the scheme and gives an overall K_D = 48 ± 8 μM, calculated from all rate constants. Fluorescence traces are the average of at least five replicate measurements (n > 5), and error bars and uncertainties given in B, C, D, F, and H denote the (propagated) standard deviation in the fitted parameter.